A new multifield determination of the galaxy luminosity function at z = 7–9 incorporating the 2012 Hubble Ultra-Deep Field imaging

Monthly Notices
of the
ROYAL ASTRONOMICAL SOCIETY

MNRAS **432,** 2696–2716 (2013)
Advance Access publication 2013 May 10

doi:10.1093/mnras/stt627

A new multifield determination of the galaxy luminosity function at $z = 7$–9 incorporating the 2012 Hubble Ultra-Deep Field imaging

R. J. McLure,[1]⋆ J. S. Dunlop,[1] R. A. A. Bowler,[1] E. Curtis-Lake,[1] M. Schenker,[2] R. S. Ellis,[2] B. E. Robertson,[3] A. M. Koekemoer,[4] A. B. Rogers,[1] Y. Ono,[5] M. Ouchi,[5] S. Charlot,[6] V. Wild,[7] D. P. Stark,[3] S. R. Furlanetto,[8] M. Cirasuolo[1] and T. A. Targett[1]

[1]*SUPA*†*, Institute for Astronomy, University of Edinburgh, Royal Observatory, Edinburgh EH9 3HJ, UK*
[2]*Department of Astrophysics, California Institute of Technology, MS 249-17, Pasadena, CA 91125, USA*
[3]*Department of Astronomy and Steward Observatory, University of Arizona, Tucson AZ 85721, USA*
[4]*Space Telescope Science Institute, 3700 San Martin Drive, Baltimore, MD 21218, USA*
[5]*Institute for Cosmic Ray Research, University of Tokyo, Kashiwa City, CHiba 277-8582, Japan*
[6]*UPMC-CNRS, UMR7095, Institut d'Astrophysique de Paris, F-75014, Paris, France*
[7]*School of Physics and Astronomy, University of St Andrews, North Haugh, St Andrews KY16 9SS, UK*
[8]*Department of Physics & Astronomy, University of California, Los Angeles, CA 90095, USA*

Accepted 2013 April 10. Received 2013 April 5; in original form 2012 December 21

ABSTRACT

We present a new determination of the ultraviolet (UV) galaxy luminosity function (LF) at redshift $z \simeq 7$ and 8, and a first estimate at $z \simeq 9$. An accurate determination of the form and evolution of the galaxy LF during this era is of key importance for improving our knowledge of the earliest phases of galaxy evolution and the process of cosmic reionization. Our analysis exploits to the full the new, deepest Wide Field Camera 3/infrared imaging from our *Hubble Space Telescope* (*HST*) Ultra-Deep Field 2012 (UDF12) campaign, with dynamic range provided by including a new and consistent analysis of all appropriate, shallower/wider area *HST* survey data. Our new measurement of the evolving LF at $z \simeq 7$ to 8 is based on a final catalogue of $\simeq$600 galaxies, and involves a step-wise maximum-likelihood determination based on the photometric redshift probability distribution for each object; this approach makes full use of the 11-band imaging now available in the Hubble Ultra-Deep Field (HUDF), including the new UDF12 F140W data, and the latest *Spitzer* IRAC imaging. The final result is a determination of the $z \simeq 7$ LF extending down to UV absolute magnitudes $M_{1500} = -16.75$ (AB mag) and the $z \simeq 8$ LF down to $M_{1500} = -17.00$. Fitting a Schechter function, we find $M^*_{1500} = -19.90^{+0.23}_{-0.28}$, $\log \phi^* = -2.96^{+0.18}_{-0.23}$ and a faint-end slope $\alpha = -1.90^{+0.14}_{-0.15}$ at $z \simeq 7$, and $M^*_{1500} = -20.12^{+0.37}_{-0.48}$, $\log \phi^* = -3.35^{+0.28}_{-0.47}$ and $\alpha = -2.02^{+0.22}_{-0.23}$ at $z \simeq 8$. These results strengthen previous suggestions that the evolution at $z > 7$ appears more akin to 'density evolution' than the apparent 'luminosity evolution' seen at $z \simeq 5 - 7$. We also provide the first meaningful information on the LF at $z \simeq 9$, explore alternative extrapolations to higher redshifts, and consider the implications for the early evolution of UV luminosity density. Finally, we provide catalogues (including derived $z_{\rm phot}$, M_{1500} and photometry) for the most robust $z \sim 6.5$-11.9 galaxies used in this analysis. We briefly discuss our results in the context of earlier work and the results derived from an independent analysis of the UDF12 data based on colour–colour selection.

Key words: galaxies: evolution – galaxies: formation – galaxies: high-redshift.

1 INTRODUCTION

The advent of deep near-infrared (IR) imaging, in particular with Wide Field Camera 3 (WFC3/IR) on the *Hubble Space Telescope* (*HST*) has now enabled the discovery and study of galaxies to be

⋆ E-mail: rjm@roe.ac.uk
† Scottish Universities Physics Alliance

extended to redshifts $z \simeq 6.5$–10, into the first billion years of cosmic history (see Dunlop 2012 for a review). This work is of fundamental importance for improving our understanding of the formation and growth of the early generations of galaxies, and testing the predictions of the latest galaxy formation simulations. It is also of interest for establishing whether these galaxies reionized the Universe (e.g. Robertson et al. 2010; Finkelstein et al. 2012; Kuhlen & Faucher-Giguére 2012), and, if so, providing more detailed information on how reionization proceeded (as compared to the integrated constraints on 'instantaneous' reionization provided by current measurements of microwave background polarization – $z_{\rm reion} \simeq 10.6 \pm 1.2$; Komatsu et al. 2011).

Because galaxies at $z \simeq 7$ are so faint, it is hard to gain detailed physical information on the properties of individual objects, and indeed only a handful of spectroscopic redshifts have been established on the basis of Lyman α (Lyα) emission at $z \simeq 7$ (the current record holder is at $z = 7.213$; Ono et al. 2012[1]). Attention has thus (sensibly) focused on population statistics, helped by the fact that significant samples of photometrically selected galaxies can now be assembled at these redshifts due to the presence of a strong Lyman break at $\lambda_{\rm rest} \simeq 1216$ Å in their spectral energy distributions (SEDs). This is caused by near-complete absorption by neutral hydrogen gas along the line of sight at $z > 6.5$ (Fan et al. 2006; Mortlock et al. 2011), making 'Lyman-break' galaxy (LBG) selection in principle straightforward at these redshifts, given adequate data.

The first and most important population measurement which is usually attempted once a significant sample of galaxies is available at a given redshift is a determination of the luminosity function (LF); i.e. the comoving number density of galaxies as a function of luminosity (≡ absolute magnitude). Prior to the 2009 installation of WFC3/IR the availability of deep z_{850} and i_{775} imaging from the Advanced Camera for Surveys (ACS) on *HST* enabled the ultraviolet (UV) ($\lambda_{\rm rest} \simeq 1500$ Å) LF to be established for faint galaxies out to $z \simeq 6$ by Bouwens et al. (2007). In a complementary effort based on the new availability of degree-scale red/IR imaging from ground-based telescopes, the bright end of the UV LF was also measured out to $z \simeq 6$ by McLure et al. (2009), who demonstrated that a combined analysis yielded a consistent result. Both of these studies exploited the available photometry to establish the presence/location of the aforementioned Lyman break, but whereas Bouwens et al. (2007) continued with the simple and well-established two colour selection technique, McLure et al. (2009) used SED fitting with evolutionary synthesis models (e.g. Bruzual & Charlot 2003) to derive photometric redshifts based on *all* of the available multiband photometry.

These two alternative approaches to galaxy selection have now both been exploited to explore the form of the LF at higher redshifts. Specifically, with the new first epoch deep WFC3/IR data provided by the Ultra-Deep Field 2009 (UDF09) programme (GO 11563, PI: Illingworth), Oesch et al. (2010a) and McLure et al. (2010) produced alternative (but again consistent) determinations of the $z \simeq 7$ galaxy UV LF. The SED fitting approach was also exploited by Finkelstein et al. (2010), while colour–colour selection has since been re-applied by Bouwens et al. (2011b) at $z \simeq 7$ and 8, to the final UDF09 data set. Colour–colour selection has also recently been applied in attempts to constrain the brighter end of the LF at $z \simeq 8$ by Bradley et al. (2012) and Oesch et al. (2012b), to the Brightest of the Reionizing Galaxies survey (BoRG)[2] and Cosmic Assembly Near-Infrared Deep Extragalactic Legacy Survey (CANDELS; Grogin et al. 2011)[3] data sets, respectively. Meanwhile, SED fitting has been applied to the UDF09 and CANDELS Great Observatories Origins Deep Survey South (GOODS-S) data by Finkelstein et al. (2012) in order to derive a new estimate of the evolving UV luminosity density, and by Bowler et al. (2012) in the search for brighter $z \simeq 7$ galaxies in the early UltraVISTA data (McCracken et al. 2012).[4]

It is important to note that, given only three filter data (i.e. two wavebands above a putative Lyman break and one below), colour–colour selection and SED fitting are essentially equivalent. However, as the number of useful wavebands expands, it is clear that SED fitting makes more complete and consistent use of the available data. This has, to some extent, been recognized by the adoption of additional criteria to colour–colour selection, in an attempt to 'factor-in' the extra information provided through other filters (e.g. the rejection of objects which shows more than one $>1.5\sigma$ detection in bluer bands and the computation of a separate $\chi^2_{\rm optical}$ by Bouwens et al. 2011b). However, SED fitting clearly deals with all detections and non-detections in a more straightforward and consistent manner, and has the additional benefit of providing actual redshift estimates with confidence intervals (and indeed can provide a redshift probability distribution for each object, albeit this depends somewhat on adopted priors; McLure et al. 2011). Finally, SED fitting also more clearly exposes the nature of potential interlopers (such as dusty red galaxies, post-starburst objects with strong Balmer breaks, and dwarf stars in our own galaxy) and provides clearer information on which data need to be improved to eliminate them (e.g. Dunlop 2012). Nevertheless, SED fitting and colour–colour selection both fundamentally rely on the Lyman break and, whatever the selection technique, careful simulation work is required to quantify selection bias, completeness and contamination in any determination of the evolving galaxy LF in the young universe.

In an attempt to make further progress, and in particular to extend the study of galaxies both to higher redshifts ($z > 8$) and lower luminosities (at $z \simeq 7$–8) we have recently completed a new programme of even deeper near-IR imaging in the Hubble Ultra-Deep Field (HUDF; Beckwith et al. 2006) with WFC3/IR on *HST*. This new imaging campaign was completed in 2012 September (GO 12498, PI: Ellis, hereafter UDF12) and when combined with the existing UDF09 data provides the deepest ever near-IR images of the sky. The data have now been reduced and released to the public (Koekemoer et al. 2013) through the team website.[5] Key elements of our observing strategy were the delivery of extremely deep Y_{105} data to more robustly identify galaxies at $z \simeq 8$ and higher redshifts, and the addition of imaging through a new filter previously unexploited in the HUDF, J_{140}, both to enable reliable galaxy discovery to be pushed beyond $z \simeq 8.5$ (with two filters longward of the Lyman break), and to enable more accurate SEDs to be determined for galaxies at $z \simeq 7$ and 8. The final UDF12+UDF09 combined data set reaches the planned 5σ detection limits of $Y_{105} = 30.0$, $J_{125} = 29.5$, $J_{140} = 29.5$ and $H_{160} = 29.5$ (in apertures of diameter 0.40, 0.44, 0.47, 0.50 arcsec, respectively, sampling 70 per cent of point source flux density in each waveband). The results of our search for galaxies at $z > 8.5$ have already been reported by Ellis et al. (2013), while the new deep multiband data have now also been exploited by Dunlop et al. (2013) in a new determination of the UV spectral slopes of galaxies at $z \simeq 7 - 9$ (with consequent implications for

[1] We note that the claimed detection of a Lyα emitter at $z = 8.55$ (Lehnert et al. 2010) now appears spurious (Bunker et al. 2013).
[2] https://wolf359.colorado.edu/
[3] http://candels.ucolick.org
[4] http://www.ultravista.org
[5] http://udf12.arizona.edu

their stellar populations). Most recently, a new determination of galaxy sizes based on the UDF12 data set has been completed by Ono et al. (2013).

In this paper, we focus on utilizing the UDF12 data set, along with the ever growing shallower WFC3/IR imaging over wider areas, to undertake a new determination of the galaxy UV LF at $z \simeq 7$ and 8. Crucially, the new ultra-deep imaging in the HUDF improves our ability to probe the faint end of the LF, better sampling the population of numerous faint galaxies ($M_{1500} > -18$) which likely dominate the UV luminosity density and hence drive reionization. A key goal, therefore, is to better establish the faint-end slope, α, on which extrapolations to even fainter (as yet unobservable) luminosities have to be based. However, simply increasing the depth of the deepest field does not yield significantly better estimates of α unless the degeneracies between the Schechter function parameters (M^*, ϕ^* and α) can be minimized (e.g. Bouwens et al. 2011b; Dunlop 2012). This requires maximizing the usable dynamic range in UV luminosity, to properly constrain the shape of the LF. Thus, to best determine the $z \simeq 7$ and 8 LF, we have analysed the new HUDF12 data in combination with the progressively shallower WFC3/IR survey data provided by the UDF09 parallel fields, the Early Release Science (ERS) data in GOODS-S, the CANDELS data in the remainder of GOODS-S and the UKIDSS Ultra-Deep Survey (UDS) field, and all of the parallel BoRG data obtained by 2012 September. In each of these fields, (including the HUDF) we have also utilized the associated *HST* ACS imaging, *Spitzer* IRAC data (deconfused with the WFC3/IR H_{160} imaging) and ground-based near-IR/optical data where appropriate.

Given that the selection functions and associated simulations are different, and to facilitate comparison with other work, our team has also undertaken a parallel, and completely independent determination of the LF at $z \simeq 7$ and 8 based on 'traditional' dropout colour–colour selection. The results from this are presented in Schenker et al. (2013) but are also summarized in this paper for ease of comparison with the SED fitting technique results derived here.

The remainder of this paper is structured as follows. In Section 2, we give full details of the data sets utilized in this new study, and explain how we selected galaxy catalogues before refining the samples to contain only plausible high-redshift galaxy candidates. We also describe the simulations undertaken to establish completeness and contamination corrections in each of the individual survey fields, simulations which are crucial for a robust determination of the LF from such a complex multifield data set. Next, in Section 3, we describe how we chose to determine the LF, adopting as our primary technique the non-parametric step-wise maximum-likelihood (SWML) method, but also applying parametric maximum-likelihood fitting to explore Schechter function representations of the LF. We then present the results of our analysis in Section 4, providing our best measurements of the LF at $z \simeq 7$, 8 and 9, and briefly exploring the implied evolution of the LF with redshift. Here, we also compare our results with the independent UDF12 analysis of Schenker et al. (2013), and discuss our derived LF parameters (with associated improved confidence intervals) in the context of the results deduced by Bouwens et al. (2011b), Bradley et al. (2012) and Oesch et al. (2012b) prior to UDF12. In Section 5, we proceed to explore the implications of our results for the evolution of the LF out to even higher redshifts, and derive the implied evolution of UV luminosity density as a function of redshift (a key measurement for tracking the likely progress of reionization). Finally, we present a summary of our conclusions in Section 6. Throughout the paper we will refer to the following *HST* ACS+WFC3/IR filters: F435W, F600LP, F606W, F775W, F814W, F850LP, F098M, F105W, F125W, F140W and F160W as B_{435}, V_{600}, V_{606}, i_{775}, i_{814}, z_{850}, Y_{098}, Y_{105}, J_{125}, J_{140} and H_{160}, respectively. All magnitudes are quoted in the AB system (Oke 1974; Oke & Gunn 1983) and all cosmological calculations assume $\Omega_0 = 0.3$, $\Omega_\Lambda = 0.7$ and $H_0 = 70$ km s^{-1} Mpc^{-1}.

2 DATA

In this section, we provide a summary of the basic properties of the data sets which we have utilized in this study to measure the high-redshift galaxy LF. In addition, we also provide details of the methods adopted to derive accurate image depth information, object photometry and reliable catalogues of high-redshift galaxy candidates.

2.1 Survey fields

The data sets analysed in this paper form a 'wedding-cake' structure ranging from the ultra-deep UDF12 observations covering an area of only $\simeq$4.5 arcmin^2 to wider area WFC3/IR survey data covering several hundred arcmin^2. Below we provide the basic observational details of each data set in turn.

2.1.1 The UDF12

The data set which plays the pivotal role in constraining the faint end of the galaxy LF at $z \geq 7$ and provides the primary motivation for this paper is the new UDF12 WFC3/IR multiband imaging of the HUDF (GO 12498, P.I. Ellis). The UDF12 observing campaign acquired 128 orbits of WFC3/IR integration time targeting the HUDF, all of which were obtained between 2012 August 4 and September 16.[6] As discussed in Section 1, the primary motivation for the UDF12 observing campaign was to improve our knowledge of number densities and spectral properties of the ultra-faint galaxy population at $z = 7$ to 8 and to provide the first robust census of the $z \geq 8.5$ galaxy population.

In order to achieve these aims the bulk of the UDF12 orbits were invested in quadrupling the HUDF integration time in the crucial Y_{105} filter and providing ultra-deep imaging in the J_{140} filter, which had not been employed in previous HUDF imaging campaigns. The 128 orbits awarded to UDF12 were allocated as follows: 72 orbits in the Y_{105} filter, 30 orbits in the J_{140} filter and 26 orbits in H_{160}. In combination with the data provided by the previous UDF09 observing campaign (GO 11563, P.I. Illingworth), the total orbit allocation of dedicated WFC3/IR data in the HUDF now stands at: 96 orbits in Y_{105}, 34 orbits in J_{125}, 30 orbits in J_{140} and 79 orbits in H_{160}. The depths of the available data in the HUDF (and the other survey fields analysed in this study) are provided inTable 1. It should be noted that the depths quoted in Table 1 have been corrected to total magnitudes assuming a point source and that the raw aperture depths are $0.2 - 0.4$ mag deeper, depending on the adopted aperture (see Section 2.3).

2.1.2 The HUDF09 parallel fields

To increase our ability to constrain the faint end of the high-redshift LF we have also utilized the WFC3/IR imaging available in the two parallel fields of the HUDF09 imaging campaign, hereafter HUDF09-1 and HUDF09-2. Although substantially shallower than

[6] The entire reduced UDF12 data set is publicly available at the following website: http://archive.stsci.edu/prepds/hudf12/

Table 1. The basic observational properties of the different WFC3/IR survey fields analysed in this work. Column 1 lists the adopted field name, columns 2 and 3 list the coordinates of the centre of the field and column 4 lists the survey area in arcmin^2. Columns 5–14 list the global average 5σ depths, which have been corrected to total magnitudes assuming a point source (a typical correction of $\simeq 0.2$ mag for ACS and $\simeq 0.4$ mag for WFC3/IR; see Section 2.3 for a discussion of the apertures adopted in each filter). It should be noted that the depths within a given field can vary significantly (e.g. CANDELS GS-DEEP and BoRG). There are no coordinates listed for BoRG simply because it consists of a large number of widely separated pointings.

Field	RA (J2000)	Dec. (J2000)	Area	B_{435}	V_{606}	i_{775}	i_{814}	z_{850}	Y_{098}	Y_{105}	J_{125}	J_{140}	H_{160}
HUDF	03:32:38.5	−27:46:57.0	4.6	29.7	30.2	29.9	–	29.1	–	29.7	29.2	29.2	29.2
HUDF09-1	03:33:01.4	−27:41:11.5	4.4	–	29.1	28.9	–	28.6	–	28.5	28.6	–	28.2
HUDF09-2	03:33:05.5	−27:51:21.6	4.5	–	29.2	29.0	29.8	28.6	–	28.6	28.7	–	28.3
CANDELS GS-WIDE	03:32:38.5	−27:53:36.5	35.1	28.0	28.4	27.8	–	27.5	–	26.9	27.1	–	26.6
ERS	03:32:23.4	−27:42:52.0	38.4	28.0	28.4	27.8	–	27.5	27.2	–	27.4	–	27.0
CANDELS GS-DEEP	03:32:29.8	−27:47:43.0	64.6	28.0	28.4	27.8	–	27.5	–	27.9	27.7	–	27.3
CANDELS UDS	02:17:25.7	−05:12:04.6	144.5	–	27.6	–	27.5	–	–	–	26.8	–	26.7
BoRG	–	–	180.4	–	27.5	–	–	–	27.8	–	26.8	–	26.8

the data available in the HUDF itself, the HUDF09 parallel fields consist of 33 and 48 WFC3/IR orbits, respectively (spread between the Y_{105}, J_{125} and H_{160} filters), and provide crucial leverage for constraining the $z \geq 7$ galaxy LF $\simeq 1.5$ mag brighter than the ultimate depth achieved by UDF12. For the purposes of this analysis, we have utilized our own reduction of the HUDF09 WFC3/IR imaging in both parallel fields (drizzled on to a 30 mas pixel scale) and have also used our own reduction of the ACS imaging covering HUDF09-2 originally obtained as part of the HUDF05 campaign (GO 10632, P.I. Stiavelli). For the HUDF and HUDF09-1 we have made use of the publicly available reductions of the original HUDF ACS imaging (Beckwith et al. 2006) and the HUDF05 ACS imaging, respectively. Finally, we have also made use of the new ultra-deep i_{814} ACS imaging (128 orbits) obtained as parallel observations during the UDF12 campaign, which provides a $\simeq$60 per cent overlap with HUDF09-2.

2.1.3 GOODS-S

In addition to the HUDF and parallel fields, we have made extensive use of the publicly available WFC3/IR imaging of the GOODS-S field provided by CANDELS (Grogin et al. 2011; Koekemoer et al. 2011). The CANDELS WFC3/IR data in GOODS-S cover a total of 24 WFC3/IR pointings which are divided into DEEP and WIDE subregions. The DEEP subregion consists of 15 WFC3/IR pointings each consisting of three orbits of Y_{105} imaging and five orbits in both J_{125} and H_{160}. The WIDE subregion consists of nine WFC3/IR pointings each consisting of a single orbit of integration in the Y_{105}, J_{125} and H_{160} filters. In addition to the CANDELS imaging, we have also analysed the ERS data in GOODS-S, which consist of 10 WFC3/IR pointings, each of which was observed for two orbits in the Y_{098}, J_{125} and H_{160} filters (Windhorst et al. 2011).

The optical data we have employed in GOODS-S are the publicly available v2.0 reduction of the original GOOD-S ACS imaging in the B_{435}, V_{606}, i_{775} and z_{850} filters (Giavalisco et al. 2004). The total area of the overlapping WFC3/IR+ACS coverage we have analysed in GOODS-S is 138 arcmin^2 (excluding the HUDF and parallel fields). A summary of the available filters and depths is provided in Table 1.

2.1.4 The UKIDSS Ultra-Deep Survey Field

In order to significantly increase the total areal coverage of our data set, crucial for constraining the bright end of the $z \geq 7$ galaxy LF, we have also analysed the publicly available CANDELS WFC3/IR+ACS imaging in the UDS (Lawrence et al. 2007). The full CANDELS data set in the UDS consists of 44 WFC3/IR pointings, each featuring 4/3 of an orbit of H_{160} imaging and 2/3 of an orbit in J_{125}. Along with the primary WFC3/IR observations, the CANDELS campaign in the UDS also obtained ACS parallels with each pixel typically receiving three orbits of integration in i_{814} and one orbit in V_{606}. However, due to the focal plane separation of the WFC3/IR and ACS cameras, only 32/44 of the WFC3/IR pointings are fully covered by the parallel ACS imaging. It is from these 32 WFC3/IR pointings, covering a total area of $\simeq$150 arcmin^2, that we have selected our sample of high-redshift candidates in the UDS.

In addition to the primary *HST* imaging data, in refining our high-redshift sample in the UDS we have also made extensive use of a variety of ground-based data sets. Amongst these the three most important are new ultra-deep z'-band imaging obtained with Suprime-Cam on *Subaru* which reaches a depth of $z' = 26.5$ (5σ; 1.8 arcsec diameter apertures), new ultra-deep VLT+HAWK-I Y-band observations of the UDS CANDELS region obtained as part of the HUGS programme (P.I. A. Fontana) which reach a depth of $Y = 26.5$ (5σ; 1.25 arcsec diameter apertures) and the latest DR10 release of the UDS K-band imaging which reaches a depth of $K = 25.1$ (5σ; 1.8 arcsec diameter apertures). Moreover, in order to clean the sample of low-redshift interlopers, we have utilized a stack of the *BVRi′ Subaru* imaging of the UDS described in Furusawa et al. (2008), which reaches a depth of $\geq$29 (2σ; 1.8 arcsec diameter apertures). Finally, in order to further refine our photometric redshift solutions we have exploited narrow-band (NB921, $\lambda_C = 9210$Å) imaging of the UDS (Sobral et al. 2011) which reaches a depth of $z_{921} = 26.0$ (5σ; 1.8 arcsec diameter apertures).

2.1.5 BoRG

In order to increase our ability to constrain the bright end of the $z = 8$ LF, we have performed our own reduction and analysis (Bowler et al., in preparation) of the data taken by the BoRG survey (Trenti et al. 2011, 2012). BoRG is a *HST* pure parallel programme, consisting of imaging in four filters from WFC3, designed to detect $z \sim 8$ LBGs as Y_{098} dropouts. Details of the BoRG observation strategy can be found in Trenti et al. (2011), however briefly, pure parallel observations were obtained at multiple sightlines in the Y_{098}, J_{125}, H_{160} filters from WFC3/IR and one or both of V_{606} and V_{600} with WFC3/UVIS. The exposure times are chosen to allow the detection of Y_{098} dropout galaxies at $z \sim 8$ based on a large $Y_{098} - J_{125}$ colour and relatively flat rest-frame spectral slope inferred from the $J_{125} - H_{160}$ colour.

At the time of writing, the complete BoRG data set consisted of 69 independent fields with a variety of different exposure times. However, to homogenize the data set somewhat, we have restricted our analysis to the 41 BoRG fields with 5σ detection limits in the range $J_{125} \geq 27.2 - 27.9$ (0.44 arcsec diameter aperture), and which lie at high galactic latitude. The calibrated FLT files were obtained from the *HST* archive and background subtracted before being combined with ASTRODRIZZLE (Gonzaga et al. 2012). The final pixel size was set to 80 mas to match the BoRG09 public reductions, using a large pix_frac (pix_frac=0.9 for multiple exposures and pix_frac = 1.0 for single exposures) to account for the lack of dithering in the observations where the primary was often spectroscopic.

Based on these 41 fields (total area 180 arcmin^2) an initial candidate list was constructed using the colour cuts employed by Bradley et al. (2012), but based on our own photometry and depth analysis (see below). As with all the other survey fields analysed here, these candidates were then analysed with our photometric redshift code before being included in the LF analysis. To mitigate the increased photometric redshift uncertainties introduced by the small number of available filters, in our final analysis of the $z = 8$ LF we include only those candidates selected from BoRG brighter than $M_{1500} \leq -20.5$.

2.2 Catalogue production

Given that the primary focus of this paper is the evolution of the galaxy LF at $z \geq 6.5$, by which point the Lyman break has been redshifted to an observed wavelength $\lambda_{obs} \geq 0.9\,\mu$m, high-redshift galaxy candidate selection was performed exclusively in the near-IR using the WFC3/IR imaging available in each field.

In order to provide a master catalogue which was as complete as possible, objects were initially selected using each individual near-IR image *and* from every possible wavelength-contiguous stack of near-IR images. For example, based on the UDF12 data, four object catalogues were generated with SEXTRACTOR v2.8.6 (Bertin & Arnouts 1996) using the individual Y_{105}, J_{125}, J_{140} and H_{160} images for object detection and a further six catalogues were generated using the following near-IR stacks as the detection image: $Y_{105} + J_{125} + J_{140} + H_{160}$, $Y_{105} + J_{125} + J_{140}$, $Y_{105} + J_{125}$, $J_{125} + J_{140}$, $J_{125} + J_{140} + H_{160}$ and $J_{140} + H_{160}$.

From this initial set of 10 object catalogues, a master catalogue was constructed containing every *unique* object which was detected at $\geq 5\sigma$ significance in any of the detection images. For those objects which were present in multiple catalogues, the positional information and photometry based on the highest signal-to-noise ratio detection was propagated to the master catalogue. Although this specific example is within the context of the UDF12 data set in the HUDF, the general selection process was identical in each field, notwithstanding differences enforced by the number of available filters.

2.3 Photometry

When selecting samples of high-redshift galaxies, the choice of photometric apertures is inevitably a balance between optimizing depth and ensuring that it is possible to derive well-defined and stable aperture corrections. The photometry adopted in this study is all based on circular apertures, where the choice of aperture in each band is tuned to enclose ≥ 70 per cent of the flux of the filter-specific point spread function (PSF). For those fields with data drizzled on to a 0.03 arcsec pix^{-1} grid, the photometry is based on 0.3 arcsec diameter apertures in the optical ACS bands and 0.40, 0.44, 0.47 and 0.50 arcsec diameter apertures in the Y_{105}, J_{125}, J_{140} and H_{160} bands. For those data sets where the data is drizzled on to a 0.06 arcsec pix^{-1} grid, we have adopted 0.40 arcsec diameter apertures in the optical ACS and Y_{098}/Y_{105} WFC3/IR bands, together with 0.44 and 0.50 arcsec diameter apertures in the J_{125} and H_{160} bands. For the purposes of the subsequent photometric redshift analysis (see below), the measured photometry in z_{850} and the WFC3/IR filters was corrected to the same enclosed flux level as the B_{435}, V_{606}, i_{775} and i_{814} photometry (typically 82–84 per cent) using the curve of growth of the observed PSFs in each band/field.

2.4 Depth analysis

A crucial element of reliable high-redshift candidate selection is the derivation of accurate information regarding the photometric depth of each available image. This information is clearly vital for the reliable exclusion of low-redshift contaminants, but is also required in order to provide the robust flux measurement errors necessary for accurate photometric redshift results.

For each survey field in turn, accurate maps of which pixels contained significant object flux were constructed by stacking SEXTRACTOR segmentation maps for each available filter. Before stacking, the individual segmentation maps were dilated in order to better capture the extended wings of bright low-redshift objects. Based on these image maps, a large number of photometric apertures (typically 10–200 thousand) were located amongst the fraction of each image that had been determined to be dominated by 'sky'. A robust estimator was then used to measure the sigma of the distribution of the fluxes measured within these sky apertures and thereby determine the empirical depth of the image for a given aperture diameter. This aperture-to-aperture rms depth measurement is a robust method of determining the actual significance of any aperture flux measurement and captures the true noise properties of a given image, which are typically underestimated by a simple measurement of the pixel rms due to small-scale noise correlations introduced by the reduction procedure (Koekemoer et al. 2013). Once the true depth of each image was determined in this fashion, the corresponding weight maps were scaled to match the empirical depth measurement. By including the scaled weight maps in the dual-mode catalogue production process, it was thereby possible to provide accurate, position dependent, flux measurement errors for each source.

2.5 High-redshift galaxy selection

In order to study the $z \geq 7$ LF it is necessary to derive reliable catalogues of $z \geq 6.5$ galaxy candidates. Consequently, the master object catalogues for each survey field were initially cleaned of low-redshift contaminants by insisting that each object remained undetected at the 2σ level in each filter shortward of the z_{850} waveband. In addition, to exclude the small number of objects with $\simeq 1.5 - 2\sigma$ detections in multiple blue optical filters, each high-redshift candidate was also required to be undetected at the 2σ level in an inverse-variance-weighted stack of all filters shortward of z_{850}.

2.5.1 Photometric redshift analysis

After the initial exclusion of low-redshift contaminants, the master catalogues for each field were processed using our photometric redshift code. For a full description of the photometric redshift code the reader is referred to McLure et al. (2011), but we provide a brief outline here for completeness. The photometry for

each galaxy is fitted with a range of galaxy templates, either empirical spectra or evolving synthetic galaxy-evolution models, with the best-fitting galaxy parameters determined via χ^2 minimization. To ensure a proper treatment of the photometric uncertainties, the model fitting is performed in flux–wavelength space, rather than magnitude–wavelength space, and negative fluxes are included.

The code fits a wide range of reddening, based on the Calzetti et al. (2000) dust attenuation law, and accounts for IGM absorption according to the Madau (1995) prescription. If necessary, the code can also fit each high-redshift candidate including additional Lyα emission within a plausible range of rest-frame equivalent widths (chosen to be $EW_0 \leq 240$ Å; Charlot & Fall 1993). The best-fitting photometric redshifts and redshift probability density functions adopted here are based on Bruzual & Charlot (2003) stellar population models with metallicities of 0.2 or $Z_\odot$, although the exact choice of stellar population model has little impact on the derived $p(z)$ in most cases. Three examples of the results of our photometric redshift analysis are shown in Fig. 1; the three objects illustrated have derived redshifts of $z \simeq 6.9$, 8.1 and 8.8 (see Table A1).

Based on the photometric redshift results, objects were excluded if it was impossible to obtain a statistically acceptable solution at $z \geq 6.5$ (typically $\chi^2_{\rm best} \geq 20$), or if the photometric redshift probability density function indicated a very low probability that the object is at $z \geq 6.5$ [i.e. $\int_{z=6.5}^{z=\infty} p(z){\rm d}z \leq 0.05$].

At this point, the catalogues were visually expected in order to remove spurious contaminants such as artefacts, diffraction spikes and overdeblended low-z objects. Following this final cleaning step, and following the procedure of McLure et al. (2011), each object was classified as *robust* or *insecure* depending on whether or not the best-fitting low-redshift solution could be ruled out at the 2σ confidence level. The objects classified as *robust* constitute our most reliable high-redshift galaxy sample and are presented in the Appendix for comparison with the results of other similar studies and potential spectroscopic follow-up observations. However, it should be noted that all high-redshift candidates which survived the full selection process, whether *robust* or *insecure*, were included in the LF analysis (see below).

2.5.2 *Dwarf star exclusion*

As has been widely discussed in the literature (e.g. Dunlop 2012; Bowler et al. 2012), ultra-cool galactic dwarf stars (M, L, & T dwarfs) are a potential source of low-redshift contamination of the bright end of the galaxy LF at $z > 6$. Within the context of the current study, the most serious source of concern is potential contamination of the $z = 7$ galaxy LF by T dwarf stars. To deal with this problem the photometry of all bright $z \simeq 7$ LBG candidates was analysed using a library of empirical optical-to-near-IR dwarf star spectra spanning the spectral range M0 to T9, taken from the SpeX archive.[7] All bright candidates which returned a high-quality fit with a dwarf star template and had a measured WFC3/IR half-light radius which was consistent with being spatially unresolved were removed from the final sample.

2.6 Final galaxy sample

The final high-redshift galaxy sample utilized in this analysis comprises a total of $N = 576$ galaxy candidates (*robust*+*insecure*) selected from a total survey area of 477 arcmin^2. The photometric redshift distribution of this sample is shown in Fig. 2. The individual redshift probability distributions, $p(z)$, of all these galaxies were used in the LF determination. In Tables A1 and A2 in the Appendix, we provide a catalogue of the 100 most robust $z \simeq 6.5 - 12.0$ galaxies uncovered within the HUDF itself (i.e. from the UDF12 data), with positions, photometry, photometric redshifts (including uncertainties), total absolute magnitudes (M_{1500}) and cross-referencing to previous studies as appropriate. The corresponding information for the robust objects in the other seven survey fields analysed here is provided in Tables A3–A9.

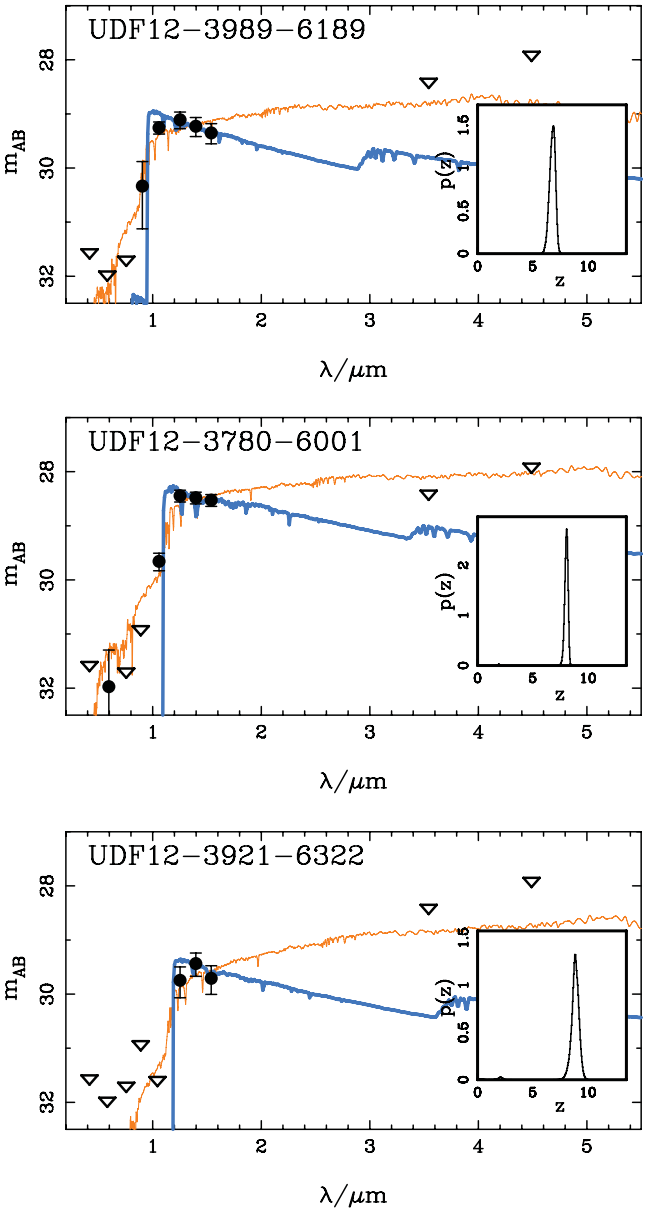

Figure 1. Examples of our photometric redshift analysis for three objects in the HUDF at redshifts $z = 6.9$, 8.1 and 8.8 (top to bottom). In each plot, the blue curve shows the best-fitting high-redshift solution, while the orange curve shows the best-fitting alternative low-redshift solution. In each case, the inset shows the photometric redshift probability density function, $p(z)$, which is incorporated into our LF analysis. The upper limits at 3.6 and 4.5 μm have been derived via our own deconfusion analysis of the ultra-deep IRAC imaging obtained by Labbé et al. (2012), using the technique described in McLure et al. (2011). All upper limits are 1σ.

[7] http://pono.ucsd.edu/ adam/browndwarfs/spexprism/

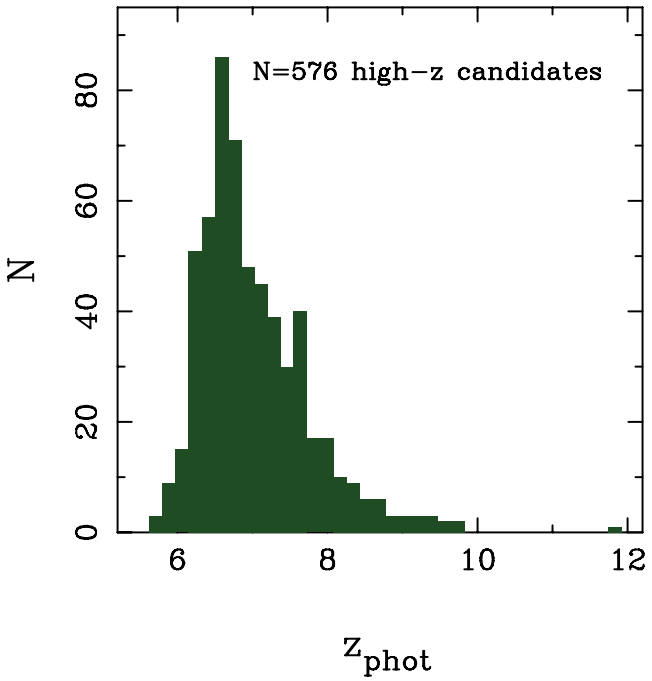

Figure 2. The photometric redshift distribution of the full sample of high-redshift galaxy candidates (*robust+insecure*) derived from our analysis of the eight survey fields listed in Table 1. The full sample consists of $N = 576$ high-redshift candidates selected from a total area of 477 arcmin^2.

We note that the advance at faint magnitudes offered by the UDF12 data set is clear, because 50 of the 100 robust $z > 6.5$ HUDF galaxies tabulated in Table A1 have not been reported in any previous study. Of these additional 50, colour–colour selection (as described by Schenker et al. 2013) finds 23 sources. The remaining 27 galaxy candidates are only revealed by our photometric redshift analysis which exploits all of the 4-band WFC3/IR imaging. Note that, for simplicity, we have decided to report only H_{160} magnitudes in Table A1, and so some *robust* objects may appear to be surprisingly faint in H_{160} because they are better detected in the shorter wavelength WFC3/IR filters.

2.7 Simulations

The final result of the object selection process is a catalogue of candidate high-redshift galaxies, each with an associated photometric redshift probability density function. However, in order to accurately derive the galaxy LF, it is then necessary to employ detailed simulations to map between the derived and intrinsic properties of each candidate.

Following the methodology of McLure et al. (2009), we adopt a parametric model of the evolving high-redshift galaxy LF in order to generate a realistic synthetic population of high-redshift galaxies. The model adopted here is a Schechter function with the three parameters (ϕ^*, $M^*_{\rm UV}$, α) evolving linearly with redshift, changing from (9.8×10^{-4} Mpc^{-3}, -20.7, -1.65) at $z = 4.5$ to (2.3×10^{-4} Mpc^{-3}, -20.1, -2.1) at $z = 9.0$. Although simple, this parametrization successfully reproduces the observed evolution of the UV-selected galaxy LF within the redshift interval $5 < z < 8$ (e.g. Bouwens et al. 2007, 2011b; McLure et al. 2009, 2010; Bradley et al. 2012).

For each survey field, the evolving LF model is used to populate an input apparent magnitude–redshift grid (m_{1500}-z, where m_{1500} is the apparent magnitude at 1500 Å), which is divided into cells of width $\delta z = 0.05$ and $\delta m_{1500} = 0.1$. For each simulated object, synthetic photometry is generated using Bruzual & Charlot (2003) galaxy templates with a range of reddening designed to produce a population of objects whose distribution of UV slopes is centred on $\beta = -2$ with a small dispersion (cf. Dunlop et al. 2012, 2013; Rogers, McLure & Dunlop 2013). The synthetic galaxies were then injected into the real data, using the empirical measurement of the WFC3/IR and ACS PSF appropriate for each individual filter. It should be noted that simulations were also conducted in which the synthetic galaxies were modelled as spatially resolved, with half-light radii drawn from the distribution measured for $z = 7$ to 8 LBGs by Oesch et al. (2010b). However, these simulations were not adopted because they were found to provide results virtually identical to the injection of PSFs and in the regime where the simulation results are most crucial for the LF determination (i.e. $M_{1500} \geq -19$) several studies indicate that the UV-selected galaxy population is virtually unresolved at the resolution of WFC3/IR (i.e. Oesch et al. 2010b; Grazian et al. 2012; Ono et al. 2013).

The simulated galaxy population was then selected and processed through our photometric redshift analysis in an identical fashion to the real sample of high-redshift galaxy candidates. The resulting $p(z)$ distribution for each synthetic galaxy was then used to populate an output m_{1500}-z grid. Under the assumption that the simulation provides a reasonable description of the actual high-redshift galaxy population, the ratio of the output and input m_{1500}-z grids provides a mapping between the observed and intrinsic properties of the high-redshift galaxy population, which automatically accounts for selection efficiency, photometric redshift errors and flux boosting.

3 LUMINOSITY FUNCTION ESTIMATION

For each survey field, the $p(z)$ distributions for each high-redshift galaxy candidate were used to populate an *observed* m_{1500}-z plane, which was then corrected using the results of the corresponding simulation to provide our best estimate of the distribution of the observed high-redshift population on the *intrinsic* m_{1500}-z plane. After aperture correcting the object magnitudes to total, it is this information that is then used to estimate the galaxy LF using two different techniques.

The primary method is an implementation of the non-parametric SWML method of Efstathiou et al. (1988). It is the results of this method which provide our basic determination of $\phi(M_{1500}, z)$, without relying on the assumption that the LF obeys a particular functional form. However, in order to compare with previous results and to study the redshift evolution of the galaxy LF, it is also desirable to derive parametric fits to the galaxy LF. Therefore, in order to derive Schechter function fits to the galaxy LF, we have also implemented a version of the parametric maximum-likelihood technique of Sandage, Tammann & Yahil (1979, hereafter STY).

When defining the likelihood, both techniques rely on the assumption that, at a given redshift, the probability of observing a galaxy of a given luminosity can be defined as follows:

$$p_i \propto \frac{\phi(L_i)}{\int_{\infty}^{L_{\rm lim}} \phi(L) {\rm d}L}, \quad (1)$$

where $L_{\rm lim}$ is the limiting luminosity of the survey. Ideally, this should be implemented in the situation where each galaxy has a unique spectroscopic redshift and luminosity. In the absence of this information, our implementation does the next best thing and adopts the normalized probability density function for each high-redshift

candidate, with the absolute UV magnitude (M_{1500}), calculated using a top-hat filter at 1500 Å in the rest frame of the best-fitting SED template, re-calculated at each step within the $p(z)$. The overall best fit is determined by maximizing the following likelihood:

$$\mathcal{L} = \prod_j \prod_i p_i, \quad (2)$$

where the outer product symbol indicates that the maximum likelihood is calculated over j separate survey fields, each with its own limiting luminosity.

One of the key strengths of both techniques is that they take no account of the absolute number density of objects and should therefore be relatively insensitive to the effects of cosmic structure. However, as a result, it is necessary to determine the overall normalization of the resulting galaxy LF estimates independently. In each case, we have derived the LF normalization by requiring that the maximum-likelihood LF estimates reproduce the cumulative number counts of observed galaxies within the appropriate redshift and absolute magnitude intervals.

4 THE GALAXY LUMINOSITY FUNCTION RESULTS

In Fig. 3, we show our new determinations of the UV-selected galaxy LFs at $z = 7$ and 8. In each panel, the data points have been derived using the SWML technique, and include error estimates which have been derived via bootstrap re-sampling of the underlying high-redshift galaxy sample. In Table 2, we provide the individual, step by step, SWML determinations of the $z = 7$ and 8 LFs and their corresponding uncertainties.

In each panel of Fig. 3, the thick red line shows our best-fitting Schechter function as derived via our implementation of the STY maximum-likelihood technique, which is constrained via a simultaneous fit to all relevant survey fields (as listed in Table 1). The confidence intervals on the derived faint-end slope and characteristic magnitude from our STY fits at $z = 7$ and 8 are shown in Fig. 4 and the best-fitting Schechter function parameters are listed in Table 3.

As can be seen from the results presented in Fig. 3, the additional dynamic range in luminosity provided by combining the new UDF12 data set with the wider area GOODS-S, CANDELS-UDS and BoRG data sets has allowed an accurate determination of the $z = 7$ and 8 LFs spanning a factor ≥50 in UV luminosity. In particular, the new UDF12 data set has allowed us to constrain the form of the LF as faint as $L \leq 0.1L^*$ for the first time. As can be seen from the results presented in Table 3, our new analysis has confirmed that the LF remains extremely steep at $M_{1500} \geq -18$ at both $z = 7$ and 8, being consistent with $\alpha = -2.0$ in both cases. Moreover, our new

Table 2. The results of our SWML determination of the $z = 7$ and 8 galaxy LFs. Columns 1 and 3 list the LF bins adopted at $z = 7$ and 8, respectively (all bins are 0.5 mag wide). Columns 2 and 4 list the individual values of ϕ_k and their corresponding uncertainties.

$z = 7$		$z = 8$	
M_{1500}	ϕ_k/mag^{-1} Mpc^{-3}	M_{1500}	ϕ_k/mag^{-1} Mpc^{-3}
−21.00	0.000 03 ± 0.000 01	−21.25	0.000 008 ± 0.000 003
−20.50	0.000 12 ± 0.000 02	−20.75	0.000 03 ± 0.000 009
−20.00	0.000 33 ± 0.000 05	−20.25	0.0001 ± 0.000 03
−19.50	0.000 75 ± 0.000 09	−19.75	0.0003 ± 0.000 06
−19.00	0.0011 ± 0.0002	−19.25	0.0005 ± 0.000 12
−18.50	0.0021 ± 0.0006	−18.75	0.0012 ± 0.0004
−18.00	0.0042 ± 0.0009	−18.25	0.0018 ± 0.0006
−17.50	0.0079 ± 0.0019	−17.75	0.0028 ± 0.0008
−17.00	0.011 ± 0.0025	−17.25	0.0050 ± 0.0025

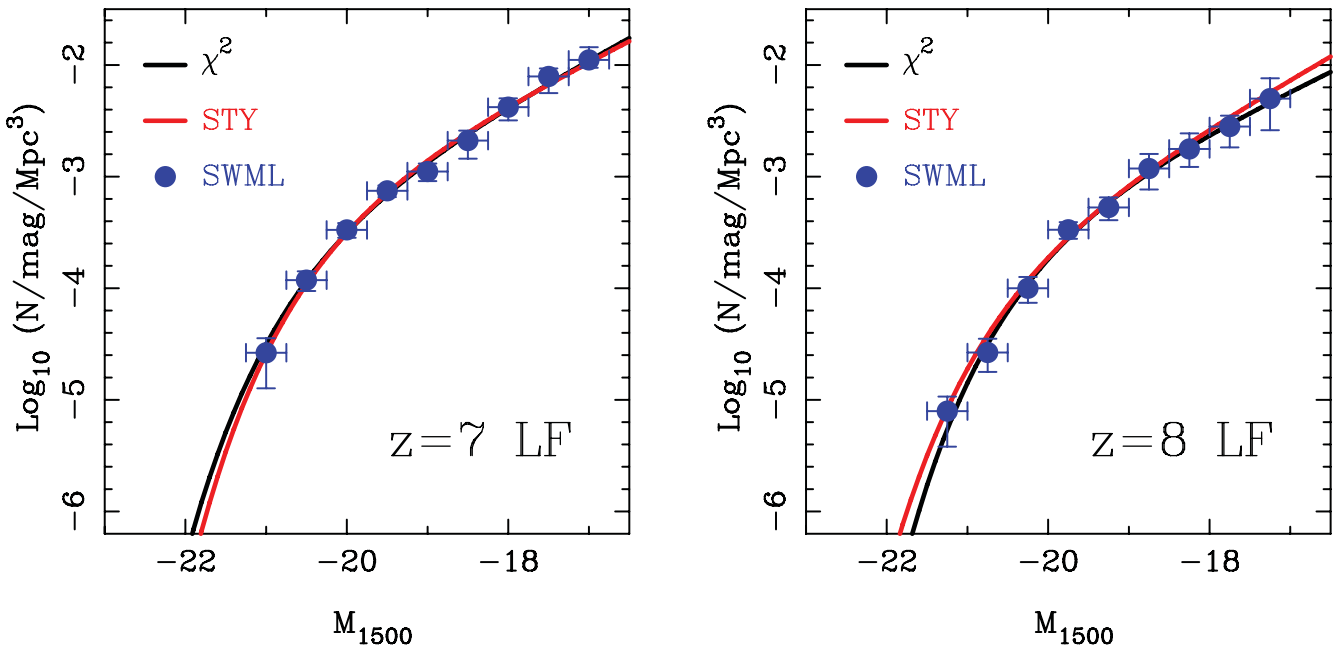

Figure 3. The left-hand panel shows our new determination of the UV-selected galaxy LF at redshift $z = 7$. The data points have been derived using a combination of our photometric redshift analysis and an implementation of the SWML method of Efstathiou, Ellis & Peterson (1988); see the text for details. The thick solid red line shows the best-fitting Schechter function derived using the parametric STY maximum-likelihood technique applied simultaneously to the first seven survey fields listed in Table 1. For comparison, we also show a straightforward χ^2 fit to the binned SWML data (thick black line). The right-hand plot shows the same information for our new determination of the $z = 8$ LF. To derive the $z = 8$ LF we have also incorporated the information derived from our own reduction and analysis of the BoRG data set.

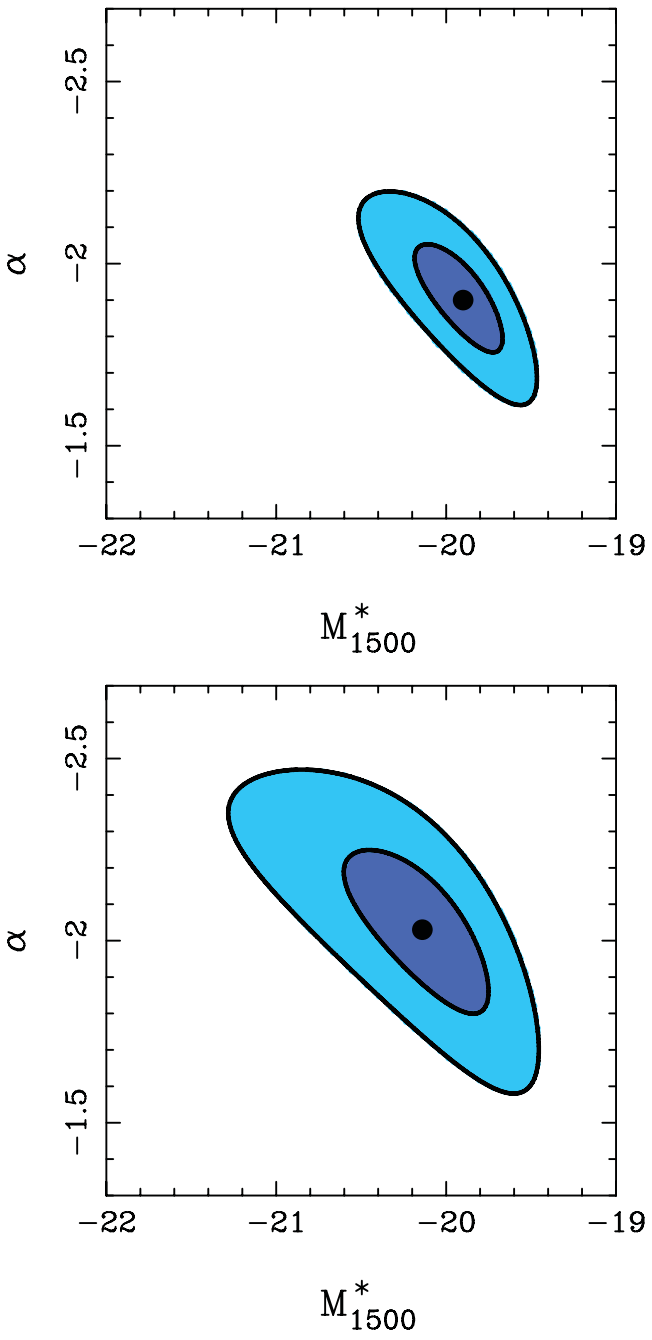

Figure 4. The confidence intervals for the faint-end slope (α) and characteristic absolute magnitude (M^*_{1500}) derived from our STY maximum-likelihood fits to the galaxy LF at $z = 7$ (top) and $z = 8$ (bottom). In each plot the 1σ and 2σ confidence intervals are illustrated by the dark and light-blue shaded areas, respectively. It should be noted that the confidence intervals plotted are based on likelihood ratios and correspond to $\Delta\chi^2 = 1$ and 4 from the best overall fit (shown by the filled circle in each case). These specific confidence intervals have been chosen in order that the corresponding one parameter uncertainties can be calculated by projecting the contours on to the relevant axis.

analysis confirms and strengthens previous results which suggested that there is little evolution in M^*_{1500} between $z = 7$ and 8. In the next section, we briefly compare our results with other relevant results in the literature, before proceeding to consider the evolution of the LF from $z \simeq 6$ to 10 and its implications for cosmic reionization.

Table 3. The Schechter function parameters for the $z = 7$ and 8 galaxy LF derived by various recent *HST* studies. The first column lists the name of the study and columns 2 to 4 list the Schechter function parameters and their quoted uncertainties. The units of ϕ^* are Mpc^{-3}.

Study	M^*_{1500}	$\log(\phi^*)$	α
$z = 7$			
This work	$-19.90^{+0.23}_{-0.28}$	$-2.96^{+0.18}_{-0.23}$	$-1.90^{+0.14}_{-0.15}$
Schenker et al. (2013)	$-20.14^{+0.36}_{-0.48}$	$-3.19^{+0.27}_{-0.24}$	$-1.87^{+0.18}_{-0.17}$
Bouwens et al. (2011b)	$-20.14^{+0.26}_{-0.26}$	$-3.07^{+0.26}_{-0.26}$	$-2.01^{+0.21}_{-0.21}$
$z = 8$			
This work	$-20.12^{+0.37}_{-0.48}$	$-3.35^{+0.28}_{-0.47}$	$-2.02^{+0.22}_{-0.23}$
Schenker et al. (2013)	$-20.44^{+0.47}_{-0.35}$	$-3.50^{+0.35}_{-0.32}$	$-1.94^{+0.21}_{-0.24}$
Bouwens et al. (2011b)	$-20.10^{+0.52}_{-0.52}$	$-3.23^{+0.43}_{-0.43}$	$-1.91^{+0.32}_{-0.32}$
Oesch et al. (2012b)	$-20.04^{+0.44}_{-0.48}$	$-3.30^{+0.38}_{-0.46}$	$-2.06^{+0.35}_{-0.28}$
Bradley et al. (2012)	$-20.26^{+0.29}_{-0.34}$	$-3.37^{+0.26}_{-0.29}$	$-1.98^{+0.23}_{-0.22}$

4.1 Comparison with previous results

Although an exhaustive comparison with previous high-redshift LF work in the literature is beyond the scope of this paper, it is instructive to compare the results derived here with those of other recent studies. Consequently, we will concentrate on a comparison between our new results and those of other recent *HST* studies which have attempted to fit all three Schechter function parameters and their corresponding uncertainties. The details of the Schechter function fits derived by the various different studies are provided in Table 3.

Given that it also includes the new UDF12 data, it is obviously of interest to compare our results to those of the companion dropout analysis of the $z = 7$ and 8 LFs performed by our team (Schenker et al. 2013). It can be seen from Table 3 that at $z = 7$ our results are in good agreement, with the extra luminosity leverage provided by UDF12 leading both studies to conclude that the faint-end slope is $\alpha = -1.9$, with a small uncertainty. The overall uncertainties on the Schechter function parameters derived in this work are slightly tighter than in Schenker et al. (2013), which is expected given that we have analysed a larger survey area. At $z = 8$ our results are again consistent with those published in Schenker et al. (2013), particularly in terms of the faint-end slope, although the value of M^*_{1500} derived by Schenker et al. is somewhat brighter than found here.

Before the start of the UDF12 imaging campaign, the most comprehensive study of the $z = 7$ and 8 LFs was performed by Bouwens et al. (2011b), who combined a dropout analysis of the WFC3/IR imaging in the HUDF09 and ERS (total area 53 arcmin^2) with constraints provided by various wider area data sets. It can be seen from Table 3 that, in terms of derived LF parameters, there is actually very good agreement between the new results derived here and those of Bouwens et al. (2011b). At some level this may be slightly fortuitous, given that the agreement between the Schechter function parameters is better than that between our respective binned SWML results and, as noted by Bouwens et al. (2011b), the small area of their study meant that their $z = 8$ faint-end slope could have been as shallow as $\alpha = -1.67 \pm 0.40$ depending on the inclusion/exclusion of two bright candidates in HUDF09-2. However, irrespective of this, it is clear that the fundamental advantage of our new analysis is the ability to better constrain the faint-end slope at both redshifts, using the deeper UDF12 imaging.

Much of the recent work in the literature has been focused on trying to improve our knowledge of the $z = 8$ LF. Within this context, two recent studies by Oesch et al. (2012b) and Bradley et al. (2012) have investigated the form of the $z = 8$ LF by combining the faint-end results of Bouwens et al. (2011b), with improved constraints at the bright end. In the case of Bradley et al. (2012), the bright-end information is provided by their dropout analysis of the BoRG WFC3/IR parallel observations, whereas in Oesch et al. (2012b) the bright-end constraints are provided by a dropout analysis of the CANDELS DEEP+WIDE imaging in GOODS-S (total area 95 arcmin^2). It can be seen from the results presented in Table 3 that, in terms of derived LF parameters, there is very good agreement between the new results derived here and those of Oesch et al. (2012b) and Bradley et al. (2012), with all studies seemingly converging on a steep faint-end slope of $\alpha \simeq -2.0$ and $M^*_{1500} \simeq -20.1$.

Overall, the comparison between derived LF parameters shown in Table 3 is therefore highly encouraging, especially given the different data sets, reductions and analysis techniques adopted by the various different studies. However, due to the fact that the current study (together with Schenker et al. 2013) exploits the deeper imaging provided by UDF12 and, uniquely, incorporates WFC3/IR imaging covering a wider area than all previous studies (including GOODS-S, CANDELS-UDS and BoRG) we are confident that the LF determination provided here is the most accurate currently available at these redshifts.

4.2 The evolution of the luminosity function

Several previous studies have concluded that the evolution of the galaxy LF over the redshift range $5 < z < 7$ can be well described as pure luminosity evolution (e.g. Bouwens et al. 2007; McLure et al. 2009; Bouwens et al. 2011b). It is clearly of some interest to investigate whether or not the evolution of the LF from $z = 7$ to 8 remains consistent with this apparently simple picture.

Some insight into this question can be gained by examining the confidence intervals on the faint-end slope and characteristic magnitude at $z = 7$ and 8 shown in Fig. 4. It can immediately be seen from Fig. 4 that our new analysis provides little evidence for a significant change in M^*_{1500} or α over the redshift interval $z = 7$ to 8 and in fact, the best-fitting Schechter function parameters (see Table 3) suggest that the dominant change is a factor of $\simeq$2.5 drop in ϕ^* between $z = 7$ and 8. We note here that Bouwens et al. (2011b) also commented that some of the $z = 7 - 8$ evolution may be explained by a change in ϕ^*, but concluded that the uncertainties were too large to be confident. Although our improved determinations of the $z = 7$ and 8 LFs strengthen the suggestion that ϕ^* is changing within the redshift range $7 < z < 8$, the results presented in Fig. 5 indicate that the available data are still insufficient to rule out pure luminosity evolution.

Given that pure luminosity evolution provides such a good description of the LF evolution over the redshift interval $4 < z < 7$ (Bouwens et al. 2011b), in Fig. 5 we explore whether a simple luminosity evolution parametrization can continue to provide an adequate description of the observed evolution at $z \geq 6$. To investigate this issue we simply fit Schechter functions to the binned SWML LF data at $z = 6$, 7 and 8, allowing M^*_{1500} to float as a free parameter, but keeping ϕ^* and α fixed at representative values ($\alpha = -1.9$ and $\phi^* = 0.00085$ Mpc^{-3}, respectively). In this simplified scenario, we find that M^*_{1500} evolves by $\simeq$0.3 mag per $\Delta z = 1$ interval, changing from $M^*_{1500} \simeq -20.3$ at $z = 6$ to $M^*_{1500} \simeq -19.7$ at $z = 8$. It is immediately clear from Fig. 5 that, within the constraints of the current data, it is still perfectly possible to reproduce the observed LF data in the redshift interval $6 < z < 8$ with pure luminosity evolution alone.

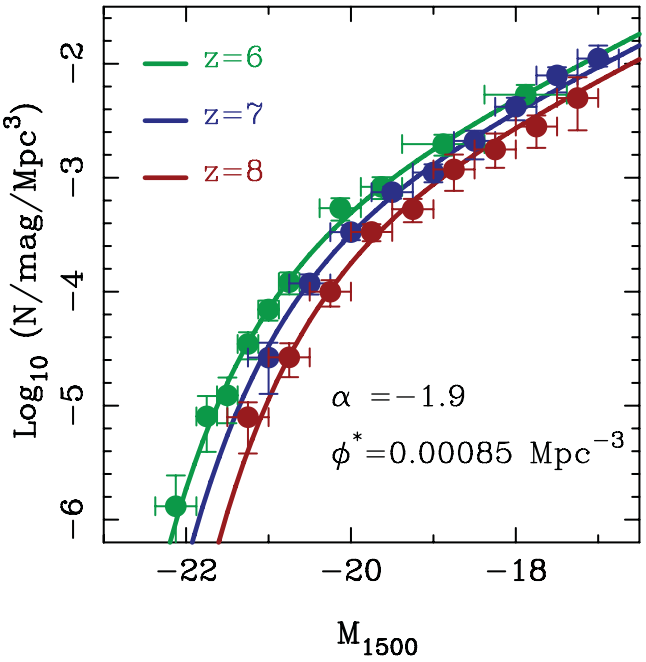

Figure 5. An illustration that pure luminosity evolution can provide an acceptable fit to the observed evolution of the galaxy LF over the redshift interval $6 < z < 8$. The blue and red data points show the SWML determination of the galaxy LF at $z = 7$ and 8 from this work, while the green data points show the determination of the $z = 6$ LF from McLure et al. (2009). The corresponding curves show the results of fitting the binned LF data with Schechter functions where the faint-end slope and overall normalization have been held constant at representative values ($\alpha = -1.9$ and $\phi^* = 0.00085$ Mpc^{-3}, respectively) but the characteristic magnitude (M^*_{1500}) has been allowed to float. In this scenario, M^*_{1500} evolves by $\simeq$0.3 mag per $\Delta z = 1$ interval, changing from $M^*_{1500} \simeq -20.3$ at $z = 6$ to $M^*_{1500} \simeq -19.7$ at $z = 8$. It can be seen that this simple parametrization is capable of satisfactorily reproducing the observed data.

4.3 The galaxy luminosity function at $z = 9$

In addition to the quadrupling of the available Y_{105} imaging in the HUDF, the key advantage provided by the new UDF12 data set is the addition of ultra-deep imaging in the previously unexploited J_{140} filter. The availability of the new J_{140} imaging provides the first real opportunity to constrain the faint end of the $z \simeq 9$ LF, simply because, in the redshift interval $8.5 < z < 9.5$, the J_{140} and H_{160} imaging still provide two filters longward of the redshifted Lyman break. Although there is significant overlap ($\simeq$2/3) between the J_{140} and H_{160} filters, the availability of two images with different noise properties is invaluable for ruling out spurious sources and avoiding the notorious problems associated with single-band detections longward of the Lyman break.

In Fig. 6, we show our SWML determination of the $z = 9$ galaxy LF, which is derived entirely from the data available in the HUDF itself. For comparison, we also show in Fig. 6 our SWML determination of the $z = 8$ LF, which is identical to that shown in Fig. 3. Although it is clearly not sensible to draw strong conclusions from two low signal-to-noise ratio LF bins, the $z = 9$ data points shown in Fig. 6 (and listed in Table 4) immediately suggest that there is no dramatic fall in the volume density of $M_{1500} \simeq -18$ galaxies

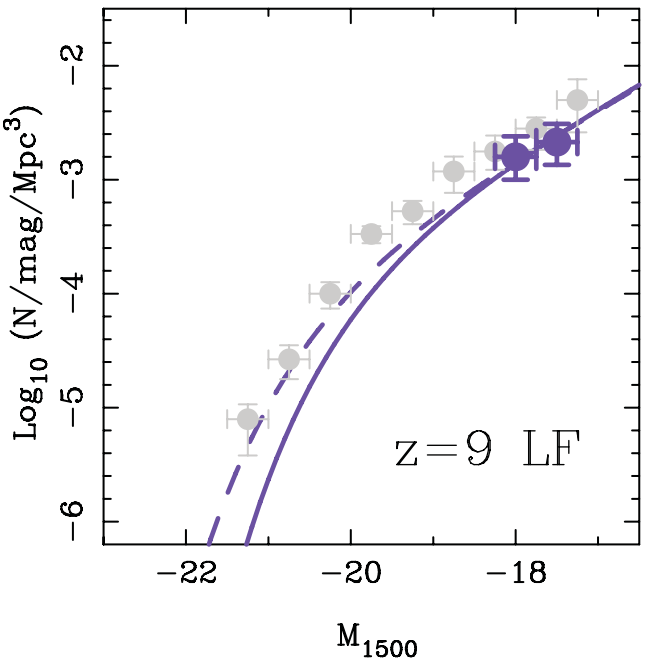

Figure 6. The large purple data points show our SWML estimate of the $z \simeq 9$ LF derived from the UDF12 data set. For context, in grey we also show our estimate of the $z = 8$ LF. The solid and dashed lines show fits to the $z = 9$ data points under the assumption that the LF evolves from $z = 8$ to 9 via pure luminosity (solid) or pure density (dashed) evolution, respectively (both assume the faint-end slope remains fixed at the $z = 8$ value). Although it is currently impossible to differentiate between them, it is clear that both scenarios would lead to very similar integrated UV luminosity densities (see the text for a discussion).

Table 4. The results of our SWML determination of two luminosity bins on the $z = 9$ galaxy LF. Column 1 lists the adopted LF bins (both are 0.5 mag wide) and column 2 lists the individual values of ϕ_k and their corresponding uncertainties.

M_{1500}	ϕ_k/mag^{-1} Mpc^{-3}
−18.00	0.0016 ± 0.0007
−17.50	0.0021 ± 0.0009

between $z = 8$ and 9. The solid and dashed lines in Fig. 6 show the result of Schechter function fits to the two $z = 9$ data points under the assumption that the evolution from $z = 8$ to 9 is either purely luminosity evolution (solid line) or purely density evolution (dashed line). In both cases, it is assumed that the LF faint-end slope remains unchanged at $\alpha = -2.02$.

It can clearly be seen from Fig. 6 that it is impossible to say anything meaningful about the *form* of any evolution of the galaxy LF between $z = 8$ and 9. However, the two alternative Schechter function fits do demonstrate that, provided the faint-end slope does not change substantially between $z = 8$ and 9, irrespective of the form of the evolution the resulting integrated UV luminosity density is likely to be very similar.

5 EVOLVING LUMINOSITY DENSITY AND COSMIC STAR FORMATION HISTORY

Given our improved knowledge of the evolving galaxy LF, it is clearly of interest to briefly explore the implications for the evolution of the observed UV luminosity density, which has a direct impact on determining whether the observed high-redshift galaxy population can reionize the Universe. For a thorough review of the constraints which could be placed on reionization pre-UDF12, the reader is referred to Robertson et al. (2010) and Finkelstein et al. (2012).

In Fig. 7, we provide a new calculation of the evolution of the observed UV luminosity density based on the McLure et al. (2009) determination of the $z = 6$ LF and the new LF determinations derived in this work at $z = 7$–9. In all cases, the data points show the results of integrating the appropriate LF down to an absolute magnitude of $M_{1500} = -17.7$, in order to allow straightforward comparison with previous work. In both panels, the right-hand axis shows how the UV luminosity density converts into a star formation rate (SFR) density under the assumption of a Salpeter initial mass function (IMF) and the conversion between UV luminosity and SFR prescribed by Madau et al. (1998). In the top panel, we show the evolution in UV luminosity density as a function of redshift, whereas in the bottom panel, we show the evolution as a function of look-back time. The upper and lower data points at $z = 10$ show how the UV luminosity density changes if the LF evolution from $z = 8$ to 9 continues to $z = 10$ as either pure luminosity (lower) or pure density evolution (upper), respectively. No dust corrections have been applied to any of the data points.

It can be seen from Fig. 7 that our data indicate that there is an order of magnitude increase in the observed UV luminosity density over the 450 Myr period between $z = 10$ and 6. Moreover, from the bottom panel of Fig. 7 it can be seen that the increase in UV density is very close to linear with cosmic time between $z = 8$ and 6. However, our new information at $z \simeq 9$ from the UDF12 data set provides some evidence that the fall-off in UV density at $z \geq 8$ is steeper than a linear trend with cosmic time, particularly if the galaxy LF continues to evolve primary via luminosity evolution. We note that in this regard our results are consistent with Oesch et al. (2012a) and the recent results from the Cluster Lensing and Supernova survey with Hubble (CLASH) campaign published by Coe et al. (2013) and Bouwens et al. (2013), which are plotted in the bottom panel of Fig. 7. A full discussion of the implications of these results within the context of cosmic reionization can be found in Robertson et al. (2013).

6 CONCLUSIONS

By combining the extreme near-IR depth provided by the UDF12 campaign with extensive wider area WFC3/IR imaging data, it has been possible to study the high-redshift galaxy LF using galaxy samples selected from a total area of $\simeq$480 arcmin^2, which span a factor of $\geq$50 in luminosity and a factor of $\simeq$1000 in number density. Based on this unique data set it has been possible to determine the most accurate measurement to date of the $z = 7$ and 8 galaxy LFs and the first meaningful constraints on the galaxy LF at $z \simeq 9$. The principal results and conclusions of our study can be summarized as follows.

(i) The extra depth provided by the UDF12 data set has allowed us to demonstrate that the faint-end slope of the galaxy LF at $z = 7$ and 8 remains extremely steep, down to $M_{1500} = -16.75$ and -17.00, respectively. Based on fitting Schechter functions, our formal

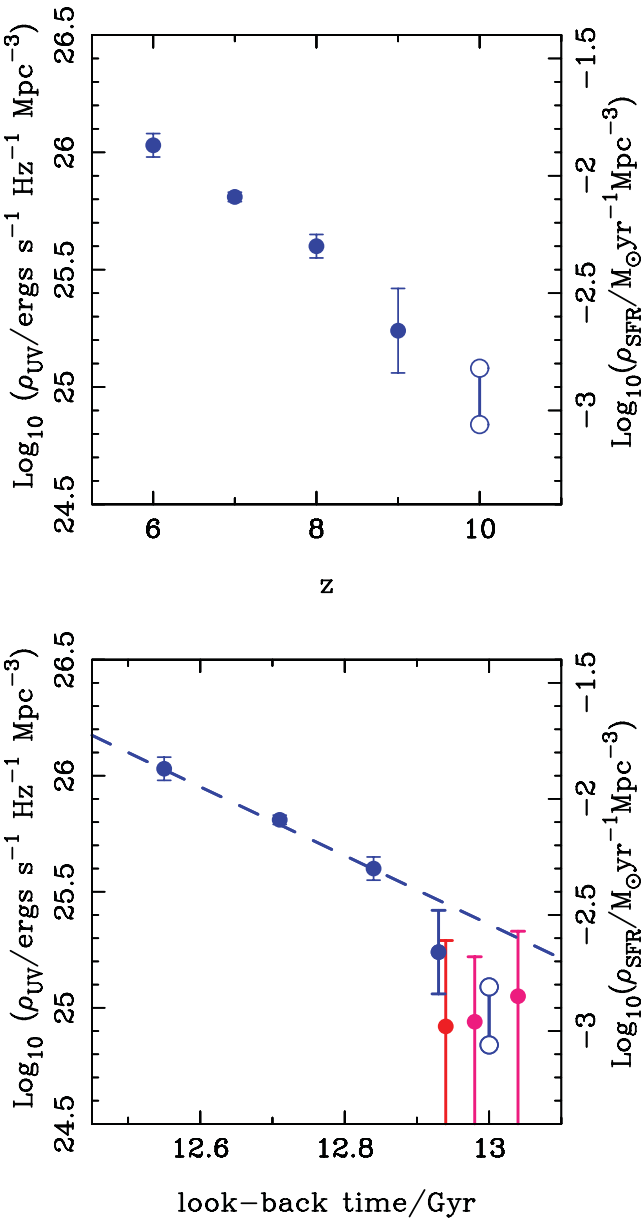

Figure 7. The evolution of the observed UV luminosity density as a function of redshift (top) and look-back time (bottom). The data points at $6 < z < 9$ show the results of integrating the galaxy LF to an absolute magnitude limit of $M_{1500} = -17.7$, where the LF parameters are taken from McLure et al. (2009) at $z = 6$ and from this work for $z = 7 - 9$. The upper and lower data points at $z = 10$ are derived by assuming that the evolution of the LF from $z = 8$ to 9 continues as either pure luminosity (lower) or pure density (upper) evolution, respectively. The dashed line shown in the bottom panel is a linear fit to the evolution of the UV luminosity density between $z = 6$ and 8. In the bottom panel, the two pink data points are the recent UV luminosity estimates from Coe et al. (2013), while the red data point is the estimate from Bouwens et al. (2013). In each panel, the right-hand axis shows how UV luminosity density converts to star formation density assuming a Salpeter IMF and the UV-to-SFR conversion of Madau, Pozzetti & Dickinson (1998).

constraints on the faint-end slope are $\alpha = -1.90^{+0.14}_{-0.15}$ at $z = 7$ and $-2.02^{+0.22}_{-0.23}$ at $z = 8$.

(ii) The results of our Schechter function fits strengthen previous suggestions that the form of the evolution of the LF between $z =$ 7 and 8 is more akin to density evolution, rather than the apparent luminosity evolution observed at redshifts $z = 5 - 7$.

(iii) However, even with the extra leverage provided by the UDF12 data set, we conclude that it is not possible to differentiate between luminosity and density evolution between $z = 7$ and 8. In fact, we demonstrate that it is perfectly possible to provide an adequate description of the observed LF data between $z = 6$ and 8 under the assumption of pure luminosity evolution alone.

(iv) The unique nature of the UDF12 data set has allowed us to place the first meaningful constraints on the faint end of the galaxy LF at $z = 9$. Taken at face value, these initial results suggest that, at least at $M_{1500} \simeq -18$, there is not a dramatic fall-off in the volume density of faint galaxies between $z = 8$ and 9.

(v) Based on our determinations of the galaxy LF within the redshift interval $6 < z < 9$, we briefly explore the evolution of the observed UV luminosity density. Our results indicate that there is an order of magnitude increase in the UV luminosity density over the redshift range $6 < z < 10$ and that between $z = 8$ and 6 the UV luminosity density increases linearly with cosmic time. However, our new results at $z \simeq 9$, together with recent results from the literature, suggest that the fall-off in UV luminosity density at $z \geq 8$ is steeper than would be expected for a linear trend with cosmic time.

ACKNOWLEDGEMENTS

RJM acknowledges the support of the European Research Council via the award of a Consolidator Grant, and the support of the Leverhulme Trust via the award of a Philip Leverhulme research prize. JSD, RAAB, TAT and VW acknowledge the support of the European Research Council via the award of an Advanced Grant to JSD. JSD also acknowledges the support of the Royal Society via a Wolfson Research Merit award. ABR and EFCL acknowledge the support of the UK Science & Technology Facilities Council. The US authors acknowledge financial support from the Space Telescope Science Institute under award HST-GO-12498.01-A. SRF is partially supported by the David and Lucile Packard Foundation. SC acknowledges the support of the European Commission through the Marie Curie Initial Training Network ELIXIR. This work is based in part on observations made with the NASA/ESA *Hubble Space Telescope*, which is operated by the Association of Universities for Research in Astronomy, Inc, under NASA contract NAS5-26555. This work is also based in part on observations made with the *Spitzer* Space Telescope, which is operated by the Jet Propulsion Laboratory, California Institute of Technology under NASA contract 1407.

REFERENCES

Beckwith S. V. W. et al., 2006, AJ, 132, 1729
Bertin E., Arnouts S., 1996, A&AS, 117, 393
Bouwens R. J., Illingworth G. D., Franx M., Ford H., 2007, ApJ, 662, 72
Bouwens R. J. et al., 2010, ApJ, 709, L133
Bouwens R. J. et al., 2011a, Nat, 469, 504
Bouwens R. J. et al., 2011b, ApJ, 737, 90
Bouwens R. J. et al., 2012, ApJ, 752, L5
Bouwens R. J. et al., 2013, ApJ, preprint (arXiv:1211.2230)
Bowler R. A. A. et al., 2012, MNRAS, 426, 2772
Bradley L. D. et al., 2012, ApJ, 760, 108
Bruzual G., Charlot S., 2003, MNRAS, 344, 1000
Bunker A. J. et al., 2010, MNRAS, 409, 855
Bunker A. J., Caruana J., Wilkins S. M., Stanway E. R., Lorenzoni S., Lacy M., Jarvis M., Hickey S., 2013, MNRAS, 430, 3314

Calzetti D., Armus L., Bohlin R. C., Kinney A. L., Koornneef J., Storchi-Bergmann T., 2000, ApJ, 533, 682
Charlot S., Fall S. M., 1993, ApJ, 415, 580
Coe D. et al., 2013, ApJ, 762, 32
Dunlop J. S., 2012, in Bromm V., Mobasher B., Wilkind T., eds, The First Galaxies - Theoretical Predictions and Observational Clues. Springer, Berlin
Dunlop J. S., McLure R. J., Robertson B. E., Ellis R. S., Stark D. P., Cirasuolo M., de Ravel L., 2012, MNRAS, 420, 901
Dunlop J. S. et al., 2013, MNRAS, in press (arXiv:1212.0860)
Efstathiou G., Ellis R. S., Peterson B. A., 1988, MNRAS, 232, 431
Ellis R. S. et al., 2013, ApJ, 763, L7
Fan X. et al., 2006, AJ, 132, 117
Finkelstein S. L., Papovich C., Giavalisco M., Reddy N. A., Ferguson H. C., Koekemoer A. M., Dickinson M., 2010, ApJ, 719, 1250
Finkelstein S. L. et al., 2012, ApJ, 756, 164
Furusawa H. et al., 2008, ApJS, 176, 1
Giavalisco M. et al., 2004, ApJ, 600, L93
Gonzaga S., Hack W., Fruchter A., Mack J., eds, 2012, The DrizzlePac Handbook. STScI, Baltimore
Grazian A. et al., 2012, A&A, 547, 51
Grogin N. A. et al., 2011, ApJS, 197, 35
Koekemoer A. M. et al., 2011, ApJS, 197, 36
Koekemoer A. M. et al., 2013, ApJS, preprint (arXiv:1212.1448)
Komatsu E. et al., 2011, ApJS, 192, 18
Kuhlen M., Faucher-Giguére C.-A., 2012, MNRAS, 423, 862
Labbé I. et al., 2012, ApJ, preprint (arXiv:1209.3037)
Lawrence A. et al., 2007, MNRAS, 379, 1599
Lehnert M. D. et al., 2010, Nat, 467, 940
Lorenzoni S., Bunker A. J., Wilkins S. M., Stanway E. R., Jarvis M. J., Caruana J., 2011, MNRAS, 414, 1455
Lorenzoni S., Bunker A. J., Wilkins S. M., Caruana J., Stanway E. R., Jarvis M. J., 2013, MNRAS, 429, 150
Madau P., 1995, ApJ, 441, 18
Madau P., Pozzetti L., Dickinson M., 1998, ApJ, 498, 106
McCracken H. J. et al., 2012, A&A, 544, 156
McLure R. J., Cirasuolo M., Dunlop J. S., Foucaud S., Almaini O., 2009, MNRAS, 395, 2196
McLure R. J., Dunlop J. S., Cirasuolo M., Koekemoer A. M., Sabbi E., Stark D., Targett T. A., Ellis R. S., 2010, MNRAS, 403, 960
McLure R. J. et al., 2011, MNRAS, 418, 2074
Mortlock D. J. et al., 2011, Nat, 474, 616
Oesch P. A. et al., 2010a, ApJ, 709, L16
Oesch P. A. et al., 2010b, ApJ, 709, L21
Oesch P. A. et al., 2012a, ApJ, 745, 110
Oesch P. A. et al., 2012b, ApJ, 759, 135
Oke J. B., 1974, ApJS, 27, 21
Oke J. B., Gunn J. E., 1983, ApJ, 266, 713
Ono Y. et al., 2012, ApJ, 744, 83
Ono Y. et al., 2013, ApJ, preprint (arXiv:1212.3869)
Ouchi M. et al., 2009, ApJ, 696, 1164
Robertson B., Ellis R. S., Dunlop J. S., McLure R. J., Stark D., 2010, Nat, 468, 49
Robertson B. et al., 2013, ApJ, 768, A71
Rogers A. B., McLure R. J., Dunlop J. S., 2013, MNRAS, 429, 2456
Sandage A., Tammann G. A., Yahil A., 1979, ApJ, 232, 352 (STY)
Schenker M. A. et al., 2013, ApJ, in press (arXiv:1212.4819)
Sobral D., Best P. N., Smail I., Geach J. E., Cirasuolo M., Garn T., Dalton G. B., 2011, MNRAS, 411, 675
Trenti M. et al., 2011, ApJ, 727, L39
Trenti M. et al., 2012, ApJ, 746, 55
Wilkins S. M., Bunker A. J., Lorenzoni S., Caruana J., 2011, MNRAS, 411, 23
Windhorst R. A. et al., 2011, ApJS, 193, 27
Yan H.-J., Windhorst R. A., Hathi N. P., Cohen S. H., Ryan R. E., O'Connell R. W., McCarthy P. J., 2010, Res. Astron. Astrophys., 10, 867
Yan H. et al., 2012, ApJ, 761, 177

APPENDIX A: ROBUST HIGH-REDSHIFT CANDIDATES

In Table A1,we provide the coordinates, photometric redshifts and absolute UV magnitudes (M_{1500}) for our $N = 100$ robust $z \geq 6.5$ galaxy candidates in the HUDF field. In Table A2, we provide the z_{850}, Y_{105}, J_{125}, J_{140} and H_{160} photometry for the same sample. In Tables A3– A9 we provide the coordinates, photometry, photometric redshifts and absolute UV magnitudes (M_{1500}) for our robust $z \geq 6.5$ galaxy candidates in the HUDF09-1, HUDF09-2, ERS, CANDELS GS-DEEP, CANDELS GS-WIDE, CANDELS UDS and BoRG fields. In all cases we quote a minimum photometric error of ± 0.1 mag, even for those objects which are detected at $\geq 10\sigma$ significance.

Table A1. Candidate $z \geq 6.5$ galaxies in the HUDF. Column 1 lists the candidate names and columns 2 and 3 list the coordinates. Columns 4 and 5 list the best-fitting photometric redshift and the corresponding 1σ uncertainty. Column 6 lists the total absolute UV magnitude, measured using a top-hat filter at 1500 Å in the rest frame of the best-fitting galaxy SED template. Column 7 lists the total apparent H_{160} magnitude (corrected to total assuming a point source). Column 8 gives references to previous discoveries of objects: (1) McLure et al. (2010), (2) Oesch et al. (2010a), (3) Finkelstein et al. (2010), (4) Bunker et al. (2010), (5) Yan et al. (2010), (6) Bouwens et al. (2010), (7) Wilkins et al. (2011) (8) Lorenzoni et al. (2011), (9) Bouwens et al. (2011b), (10) Bouwens et al. (2011b) potential, (11) McLure et al. (2011), (12) Bouwens et al. (2011a) and (13) Schenker et al. (2013).

Name	RA(J2000)	Dec.(J2000)	$z_{\rm phot}$	Δz	M_{1500}	H_{160}	References
UDF12-3999-6197	03:32:39.99	−27:46:19.7	6.5	6.2–7.1	−17.5	$28.8^{+0.1}_{-0.1}$	
UDF12-3696-5536	03:32:36.96	−27:45:53.6	6.5	6.1–6.9	−17.5	$29.5^{+0.3}_{-0.2}$	9, 13
UDF12-3677-7536	03:32:36.77	−27:47:53.6	6.5	6.4–6.6	−19.0	$27.8^{+0.1}_{-0.1}$	1, 2, 3, 7, 9, 11, 13
UDF12-3897-8116	03:32:38.97	−27:48:11.6	6.5	6.1–7.0	−17.4	$29.4^{+0.3}_{-0.2}$	13
UDF12-4120-6561	03:32:41.20	−27:46:56.1	6.5	6.3–6.9	−16.9	>30.2	
UDF12-3515-7257	03:32:35.15	−27:47:25.7	6.5	6.3–6.8	−17.4	$29.7^{+0.4}_{-0.3}$	
UDF12-3909-6092	03:32:39.09	−27:46:09.2	6.5	6.3–6.8	−17.5	$29.5^{+0.3}_{-0.2}$	13
UDF12-3865-6041	03:32:38.65	−27:46:04.1	6.6	6.3–6.8	−17.8	$29.4^{+0.3}_{-0.2}$	
UDF12-3702-5534	03:32:37.02	−27:45:53.4	6.6	6.2–6.9	−17.2	$30.2^{+0.6}_{-0.4}$	9
UDF12-3922-6148	03:32:39.22	−27:46:14.8	6.6	6.2–7.0	−17.2	$29.7^{+0.4}_{-0.3}$	13
UDF12-3736-6245	03:32:37.36	−27:46:24.5	6.6	6.3–6.9	−17.7	$29.2^{+0.2}_{-0.2}$	9, 13

Table A1 – *continued*

Name	RA(J2000)	Dec.(J2000)	$z_{\rm phot}$	Δz	M_{1500}	H_{160}	References
UDF12-4379-6511	03:32:43.79	−27:46:51.1	6.6	6.4–6.8	−17.7	$29.4^{+0.3}_{-0.2}$	13
UDF12-3859-6521	03:32:38.59	−27:46:52.1	6.6	6.4–6.8	−17.8	$29.2^{+0.2}_{-0.2}$	9, 13
UDF12-4202-7074	03:32:42.02	−27:47:07.4	6.6	6.3–7.0	−17.6	$29.1^{+0.2}_{-0.2}$	13
UDF12-3638-7163	03:32:36.38	−27:47:16.3	6.6	6.4–6.7	−18.7	$28.2^{+0.1}_{-0.1}$	1, 2, 3, 4, 5, 7, 9, 11, 13
UDF12-4254-6481	03:32:42.54	−27:46:48.1	6.6	6.3–6.9	−17.1	$30.2^{+0.7}_{-0.4}$	
UDF12-4058-5570	03:32:40.58	−27:45:57.0	6.6	6.3–6.8	−18.0	$29.1^{+0.2}_{-0.2}$	
UDF12-3858-6150	03:32:38.58	−27:46:15.0	6.6	5.9–7.4	−17.1	$29.7^{+0.4}_{-0.3}$	
UDF12-4186-6322	03:32:41.86	−27:46:32.2	6.6	6.2–7.0	−17.8	$29.0^{+0.2}_{-0.2}$	9
UDF12-4144-7041	03:32:41.44	−27:47:04.1	6.6	6.1–7.0	−17.4	$29.6^{+0.4}_{-0.3}$	13
UDF12-4288-6261	03:32:42.88	−27:46:26.1	6.6	6.3–6.9	−17.4	$30.1^{+0.6}_{-0.4}$	13
UDF12-3900-6482	03:32:39.00	−27:46:48.2	6.6	6.4–7.0	−18.3	$28.2^{+0.1}_{-0.1}$	
UDF12-4182-6112	03:32:41.82	−27:46:11.2	6.7	6.4–7.1	−18.1	$28.5^{+0.1}_{-0.1}$	3, 7, 7, 9, 11, 13
UDF12-4268-7073	03:32:42.68	−27:47:07.3	6.7	6.4–7.0	−18.3	$28.5^{+0.1}_{-0.1}$	13
UDF12-3734-7192	03:32:37.34	−27:47:19.2	6.7	6.4–6.9	−18.0	$29.1^{+0.2}_{-0.2}$	13
UDF12-3968-6066	03:32:39.68	−27:46:06.6	6.7	6.2–7.2	−17.1	>30.2	9
UDF12-4219-6278	03:32:42.19	−27:46:27.8	6.7	6.6–6.9	−19.2	$27.7^{+0.1}_{-0.1}$	1, 3, 7, 9, 11, 13
UDF12-3796-6020	03:32:37.96	−27:46:02.0	6.7	6.3–7.1	−17.5	$29.5^{+0.3}_{-0.2}$	
UDF12-3675-6447	03:32:36.75	−27:46:44.7	6.7	6.4–7.3	−18.1	$28.7^{+0.1}_{-0.1}$	
UDF12-3744-6513	03:32:37.44	−27:46:51.3	6.7	6.6–6.9	−19.0	$28.1^{+0.1}_{-0.1}$	1, 2, 3, 5, 7, 9, 11, 13
UDF12-4160-7045	03:32:41.60	−27:47:04.5	6.7	6.5–6.9	−18.5	$28.4^{+0.1}_{-0.1}$	9, 11, 13
UDF12-4122-7232	03:32:41.22	−27:47:23.2	6.8	6.5–7.0	−17.7	$29.3^{+0.3}_{-0.2}$	
UDF12-3894-7456	03:32:38.94	−27:47:45.6	6.8	6.4–7.1	−17.3	$29.5^{+0.3}_{-0.3}$	
UDF12-4290-7174	03:32:42.90	−27:47:17.4	6.8	6.4–7.2	−17.3	$30.2^{+0.7}_{-0.4}$	
UDF12-4056-6436	03:32:40.56	−27:46:43.6	6.8	6.7–7.0	−18.7	$28.3^{+0.1}_{-0.1}$	1, 2, 3, 4, 5, 7, 9, 11, 13
UDF12-4431-6452	03:32:44.31	−27:46:45.2	6.8	6.6–7.0	−18.7	$28.4^{+0.1}_{-0.1}$	1, 9, 11, 13
UDF12-3958-6565	03:32:39.58	−27:46:56.5	6.8	6.6–7.0	−18.9	$28.0^{+0.1}_{-0.1}$	1, 2, 3, 5, 9, 11, 13
UDF12-4037-6560	03:32:40.37	−27:46:56.0	6.8	6.5–7.1	−17.5	$29.7^{+0.4}_{-0.3}$	9, 13
UDF12-4019-6190	03:32:40.19	−27:46:19.0	6.9	6.5–7.2	−17.5	$29.4^{+0.3}_{-0.2}$	13
UDF12-4422-6337	03:32:44.22	−27:46:33.7	6.9	6.4–7.3	−17.1	$30.2^{+0.8}_{-0.4}$	
UDF12-4472-6362	03:32:44.72	−27:46:36.2	6.9	6.5–7.1	−18.3	$28.3^{+0.1}_{-0.1}$	13
UDF12-4263-6416	03:32:42.63	−27:46:41.6	6.9	6.5–7.2	−17.3	$29.8^{+0.4}_{-0.3}$	13
UDF12-4484-6568	03:32:44.84	−27:46:56.8	6.9	6.5–7.1	−17.9	$29.2^{+0.4}_{-0.3}$	
UDF12-3975-7451	03:32:39.75	−27:47:45.1	6.9	6.4–7.1	−18.1	$29.0^{+0.2}_{-0.2}$	9, 13
UDF12-3989-6189	03:32:39.89	−27:46:18.9	6.9	6.5–7.1	−18.0	$29.1^{+0.2}_{-0.2}$	1, 13
UDF12-3729-6175	03:32:37.29	−27:46:17.5	6.9	6.5–7.1	−18.2	$28.5^{+0.1}_{-0.1}$	10
UDF12-3456-6494	03:32:34.56	−27:46:49.4	7.0	6.6–7.3	−17.9	$28.8^{+0.1}_{-0.1}$	9, 13
UDF12-4068-6498	03:32:40.68	−27:46:49.8	7.0	6.3–7.4	−17.9	$29.2^{+0.2}_{-0.2}$	13
UDF12-3692-6516	03:32:36.92	−27:46:51.6	7.0	6.6–7.4	−17.5	$29.9^{+0.5}_{-0.3}$	10, 13
UDF12-4071-7347	03:32:40.71	−27:47:34.7	7.0	6.8–7.3	−17.8	$29.7^{+0.4}_{-0.3}$	9, 13
UDF12-4036-8022	03:32:40.36	−27:48:02.2	7.0	6.6–7.4	−17.3	$30.2^{+0.8}_{-0.5}$	3, 9, 13
UDF12-3755-6019	03:32:37.55	−27:46:01.9	7.1	6.7–7.4	−17.6	$29.2^{+0.2}_{-0.2}$	9, 13
UDF12-4256-6566	03:32:42.56	−27:46:56.6	7.1	7.0–7.2	−20.3	$26.5^{+0.1}_{-0.1}$	1, 2, 3, 4, 5, 7, 9, 11, 13
UDF12-4105-7156	03:32:41.05	−27:47:15.6	7.1	6.8–7.3	−19.0	$28.0^{+0.1}_{-0.1}$	1, 2, 3, 5, 13
UDF12-3853-7519	03:32:38.53	−27:47:51.9	7.1	6.9–7.3	−18.0	$29.3^{+0.3}_{-0.2}$	2, 4, 13
UDF12-3825-6566	03:32:38.25	−27:46:56.6	7.1	6.6–7.6	−17.5	$29.4^{+0.3}_{-0.2}$	
UDF12-3836-6119	03:32:38.36	−27:46:11.9	7.1	6.8–7.3	−18.8	$28.2^{+0.1}_{-0.1}$	3, 4, 5, 9, 11

Table A1 – *continued*

Name	RA(J2000)	Dec.(J2000)	$z_{\rm phot}$	Δz	M_{1500}	H_{160}	References
UDF12-3709-6441	03:32:37.09	−27:46:44.1	7.2	6.6–7.6	−17.0	$29.8^{+0.4}_{-0.3}$	
UDF12-3402-6504	03:32:34.02	−27:46:50.4	7.2	6.9–7.3	−18.4	$28.8^{+0.1}_{-0.1}$	9, 13
UDF12-4384-6311	03:32:43.84	−27:46:31.1	7.2	6.9–7.5	−17.9	$29.5^{+0.3}_{-0.2}$	13
UDF12-4256-7314	03:32:42.56	−27:47:31.4	7.2	7.1–7.4	−19.6	$27.3^{+0.1}_{-0.1}$	1, 2, 3, 4, 5, 7, 9, 13
UDF12-4035-7468	03:32:40.35	−27:47:46.8	7.2	6.7–7.6	−17.5	$29.8^{+0.4}_{-0.3}$	
UDF12-3973-6214	03:32:39.73	−27:46:21.4	7.3	7.1–7.4	−18.4	$28.8^{+0.1}_{-0.1}$	1, 2, 3, 4, 5, 8, 9, 11
UDF12-3668-8067	03:32:36.68	−27:48:06.7	7.3	7.0–7.5	−18.1	$29.3^{+0.3}_{-0.2}$	9
UDF12-3708-8092	03:32:37.08	−27:48:09.2	7.3	6.6–7.7	−17.5	$29.5^{+0.4}_{-0.3}$	
UDF12-4242-6243	03:32:42.42	−27:46:24.3	7.3	7.0–7.5	−18.4	$28.5^{+0.1}_{-0.1}$	3, 5, 9
UDF12-3431-7115	03:32:34.31	−27:47:11.5	7.3	7.0–7.5	−18.6	$28.1^{+0.1}_{-0.1}$	
UDF12-3868-5477	03:32:38.68	−27:45:47.7	7.3	6.7–7.8	−17.1	$29.9^{+0.4}_{-0.3}$	
UDF12-4242-6137	03:32:42.42	−27:46:13.7	7.3	6.9–7.7	−18.1	$28.8^{+0.2}_{-0.2}$	
UDF12-4100-7216	03:32:41.00	−27:47:21.6	7.3	6.8–7.8	−17.3	>30.2	13
UDF12-4239-6243	03:32:42.39	−27:46:24.3	7.3	7.0–7.5	−18.4	$28.7^{+0.2}_{-0.2}$	3, 5, 9, 13
UDF12-4314-6285	03:32:43.14	−27:46:28.5	7.3	6.8–7.5	−19.1	$27.7^{+0.1}_{-0.1}$	1, 2, 3, 4, 5, 6, 7, 9, 11, 13
UDF12-3313-6545	03:32:33.13	−27:46:54.5	7.4	7.2–7.6	−18.6	$28.6^{+0.1}_{-0.1}$	1, 4, 5, 9, 11, 13
UDF12-3885-7540	03:32:38.85	−27:47:54.0	7.5	7.1–7.7	−18.2	$28.9^{+0.2}_{-0.2}$	
UDF12-3931-6181	03:32:39.31	−27:46:18.1	7.5	7.3–7.8	−18.2	$29.2^{+0.2}_{-0.2}$	13
UDF12-4334-6252	03:32:43.34	−27:46:25.2	7.5	7.0–8.0	−17.4	$30.2^{+0.7}_{-0.4}$	
UDF12-4308-6242	03:32:43.08	−27:46:24.2	7.6	7.1–7.9	−17.7	$29.2^{+0.2}_{-0.2}$	1, 9, 11, 13
UDF12-3880-7072	03:32:38.80	−27:47:07.2	7.7	7.5–7.8	−20.1	$26.8^{+0.1}_{-0.1}$	1, 2, 3, 4, 5, 7, 9, 11, 13
UDF12-4281-6505	03:32:42.81	−27:46:50.5	7.7	7.2–8.0	−17.9	$28.9^{+0.2}_{-0.1}$	
UDF12-4288-6345	03:32:42.88	−27:46:34.5	7.7	7.5–7.9	−18.9	$27.9^{+0.1}_{-0.1}$	1, 3, 4, 5, 6, 8, 9, 11
UDF12-4470-6443	03:32:44.70	−27:46:44.3	7.7	7.6–7.9	−19.7	$27.4^{+0.1}_{-0.1}$	1, 2, 3, 4, 5, 9, 11, 13
UDF12-4033-8026	03:32:40.33	−27:48:02.6	7.7	7.5–8.0	−18.0	$29.0^{+0.2}_{-0.2}$	3, 9, 13
UDF12-3722-8061	03:32:37.22	−27:48:06.1	7.7	7.5–7.9	−19.2	$27.9^{+0.1}_{-0.1}$	1, 2, 3, 4, 5, 9, 11, 13
UDF12-4474-6449	03:32:44.74	−27:46:44.9	7.8	7.5–7.9	−18.5	$28.8^{+0.1}_{-0.1}$	1, 3, 5, 13
UDF12-4240-6550	03:32:42.40	−27:46:55.0	7.8	7.5–8.1	−17.9	$29.1^{+0.2}_{-0.2}$	9, 13
UDF12-3939-7040	03:32:39.39	−27:47:04.0	7.8	7.6–8.1	−18.4	$28.5^{+0.1}_{-0.1}$	13
UDF12-3911-6493	03:32:39.11	−27:46:49.3	7.9	7.5–8.2	−18.0	$29.2^{+0.2}_{-0.2}$	9
UDF12-3344-6598	03:32:33.44	−27:46:59.8	7.9	7.6–8.1	−18.1	$29.0^{+0.2}_{-0.2}$	9
UDF12-3952-7174	03:32:39.52	−27:47:17.4	7.9	7.8–8.0	−19.3	$27.6^{+0.1}_{-0.1}$	1, 2, 3, 4, 5, 7, 9, 11, 13
UDF12-4308-6277	03:32:43.08	−27:46:27.7	8.0	7.8–8.1	−18.4	$28.9^{+0.2}_{-0.1}$	1, 3, 5, 6, 7, 8, 9, 11, 13
UDF12-3780-6001	03:32:37.80	−27:46:00.1	8.1	7.9–8.2	−18.9	$28.3^{+0.1}_{-0.1}$	1, 3, 4, 5, 6, 8, 9, 13
UDF12-3917-5449	03:32:39.17	−27:45:44.9	8.1	7.8–8.5	−17.4	$29.7^{+0.4}_{-0.3}$	
UDF12-3762-6011	03:32:37.62	−27:46:01.1	8.1	7.9–8.4	−17.9	$29.4^{+0.3}_{-0.2}$	
UDF12-3813-5540	03:32:38.13	−27:45:54.0	8.3	8.2–8.5	−19.1	$28.0^{+0.1}_{-0.1}$	1, 3, 4, 5, 6, 8, 9, 11, 13
UDF12-3763-6015	03:32:37.63	−27:46:01.5	8.3	8.1–8.5	−18.7	$28.4^{+0.1}_{-0.1}$	1, 3, 4, 5, 6, 9, 13
UDF12-3947-8076	03:32:39.47	−27:48:07.6	8.6	8.4–8.8	−18.6	$28.6^{+0.1}_{-0.1}$	9
UDF12-3921-6322	03:32:39.21	−27:46:32.2	8.8	8.6–9.2	−18.0	$29.5^{+0.3}_{-0.2}$	13
UDF12-4344-6547	03:32:43.44	−27:46:54.7	8.8	8.3–9.3	−17.6	$29.7^{+0.4}_{-0.3}$	13
UDF12-4265-7049	03:32:42.65	−27:47:04.9	9.5	8.8–9.9	−18.1	$29.3^{+0.2}_{-0.2}$	
UDF12-3954-6285	03:32:39.54	−27:46:28.5	11.9	11.4–12.2	−19.7	$28.9^{+0.2}_{-0.1}$	12

Table A2. Optical and near-IR photometry for the candidate $z \geq 6.5$ galaxies in the HUDF. In each case, the quoted photometry has been corrected to total assuming a point source. Detections which are less significant than 2σ are listed as the appropriate 2σ limit. All candidates are detected at less than 2σ significance in the B_{435}, V_{606} and i_{775} filters.

Name	z_{850}	Y_{105}	J_{125}	J_{140}	H_{160}
UDF12-3999-6197	>30.1	$29.4^{+0.2}_{-0.1}$	$29.3^{+0.2}_{-0.2}$	$29.5^{+0.3}_{-0.3}$	$28.8^{+0.1}_{-0.1}$
UDF12-3696-5536	>30.1	$29.3^{+0.2}_{-0.2}$	$29.4^{+0.3}_{-0.2}$	$28.8^{+0.2}_{-0.2}$	$29.5^{+0.3}_{-0.2}$
UDF12-3677-7536	$28.6^{+0.2}_{-0.1}$	$27.8^{+0.1}_{-0.1}$	$27.8^{+0.1}_{-0.1}$	$27.9^{+0.1}_{-0.1}$	$27.8^{+0.1}_{-0.1}$
UDF12-3897-8116	>30.1	$29.4^{+0.2}_{-0.2}$	$29.3^{+0.3}_{-0.2}$	$29.7^{+0.4}_{-0.3}$	$29.4^{+0.3}_{-0.2}$
UDF12-4120-6561	>30.0	$29.6^{+0.2}_{-0.2}$	$30.2^{+0.8}_{-0.4}$	$30.0^{+0.5}_{-0.4}$	>30.2
UDF12-3515-7257	>30.1	$29.3^{+0.2}_{-0.1}$	$29.6^{+0.3}_{-0.3}$	$29.5^{+0.3}_{-0.3}$	$29.7^{+0.4}_{-0.3}$
UDF12-3909-6092	$30.8^{+0.7}_{-0.4}$	$29.1^{+0.1}_{-0.1}$	$29.3^{+0.3}_{-0.2}$	$29.9^{+0.5}_{-0.3}$	$29.5^{+0.3}_{-0.2}$
UDF12-3865-6041	$29.8^{+0.5}_{-0.4}$	$29.0^{+0.1}_{-0.1}$	$29.0^{+0.2}_{-0.2}$	$29.1^{+0.2}_{-0.2}$	$29.4^{+0.3}_{-0.2}$
UDF12-3702-5534	>30.1	$29.6^{+0.2}_{-0.2}$	$29.6^{+0.3}_{-0.3}$	$29.9^{+0.5}_{-0.3}$	$30.2^{+0.6}_{-0.4}$
UDF12-3922-6148	>30.1	$29.5^{+0.2}_{-0.2}$	$29.8^{+0.4}_{-0.3}$	$30.1^{+0.6}_{-0.4}$	$29.7^{+0.4}_{-0.3}$
UDF12-3736-6245	>30.1	$29.1^{+0.1}_{-0.1}$	$29.1^{+0.2}_{-0.2}$	$29.1^{+0.2}_{-0.2}$	$29.2^{+0.2}_{-0.2}$
UDF12-4379-6511	>30.1	$29.0^{+0.1}_{-0.1}$	$29.5^{+0.3}_{-0.3}$	$29.3^{+0.3}_{-0.2}$	$29.4^{+0.3}_{-0.2}$
UDF12-3859-6521	>30.1	$29.0^{+0.1}_{-0.1}$	$29.0^{+0.2}_{-0.2}$	$29.6^{+0.3}_{-0.3}$	$29.2^{+0.2}_{-0.2}$
UDF12-4202-7074	>30.1	$29.2^{+0.1}_{-0.1}$	$29.2^{+0.2}_{-0.2}$	$29.5^{+0.3}_{-0.2}$	$29.1^{+0.2}_{-0.2}$
UDF12-3638-7163	$29.1^{+0.2}_{-0.2}$	$28.1^{+0.1}_{-0.1}$	$28.1^{+0.1}_{-0.1}$	$28.0^{+0.1}_{-0.1}$	$28.2^{+0.1}_{-0.1}$
UDF12-4254-6481	>30.1	$29.6^{+0.2}_{-0.2}$	$29.9^{+0.5}_{-0.3}$	$29.9^{+0.5}_{-0.3}$	$30.2^{+0.7}_{-0.4}$
UDF12-4058-5570	$29.7^{+0.5}_{-0.3}$	$28.9^{+0.1}_{-0.1}$	$28.7^{+0.2}_{-0.1}$	$29.0^{+0.2}_{-0.2}$	$29.1^{+0.2}_{-0.2}$
UDF12-3858-6150	>30.1	$29.9^{+0.3}_{-0.2}$	$29.5^{+0.3}_{-0.2}$	$30.0^{+0.6}_{-0.4}$	$29.7^{+0.4}_{-0.3}$
UDF12-4186-6322	$29.9^{+0.6}_{-0.4}$	$29.1^{+0.1}_{-0.1}$	$28.9^{+0.2}_{-0.1}$	$29.4^{+0.3}_{-0.2}$	$29.0^{+0.2}_{-0.2}$
UDF12-4144-7041	>30.1	$29.5^{+0.2}_{-0.2}$	$29.3^{+0.3}_{-0.2}$	$29.8^{+0.5}_{-0.3}$	$29.6^{+0.4}_{-0.3}$
UDF12-4288-6261	>30.0	$29.4^{+0.2}_{-0.1}$	$29.5^{+0.3}_{-0.2}$	$29.7^{+0.4}_{-0.3}$	$30.1^{+0.6}_{-0.4}$
UDF12-3900-6482	$30.0^{+0.7}_{-0.4}$	$28.7^{+0.1}_{-0.1}$	$28.6^{+0.1}_{-0.1}$	$28.4^{+0.1}_{-0.1}$	$28.2^{+0.1}_{-0.1}$
UDF12-4182-6112	$30.1^{+0.8}_{-0.4}$	$28.9^{+0.1}_{-0.1}$	$28.7^{+0.1}_{-0.1}$	$28.6^{+0.1}_{-0.1}$	$28.5^{+0.1}_{-0.1}$
UDF12-4268-7073	$29.7^{+0.5}_{-0.3}$	$28.7^{+0.1}_{-0.1}$	$28.5^{+0.1}_{-0.1}$	$28.4^{+0.1}_{-0.1}$	$28.5^{+0.1}_{-0.1}$
UDF12-3734-7192	>30.1	$28.9^{+0.1}_{-0.1}$	$28.9^{+0.2}_{-0.1}$	$29.1^{+0.2}_{-0.2}$	$29.1^{+0.2}_{-0.2}$
UDF12-3968-6066	>30.1	$29.8^{+0.3}_{-0.2}$	$29.4^{+0.3}_{-0.2}$	$29.7^{+0.4}_{-0.3}$	>30.2
UDF12-4219-6278	$28.9^{+0.2}_{-0.2}$	$27.7^{+0.1}_{-0.1}$	$27.7^{+0.1}_{-0.1}$	$27.6^{+0.1}_{-0.1}$	$27.7^{+0.1}_{-0.1}$
UDF12-3796-6020	>30.1	$29.4^{+0.2}_{-0.1}$	$29.3^{+0.3}_{-0.2}$	$29.4^{+0.3}_{-0.2}$	$29.5^{+0.3}_{-0.2}$
UDF12-3675-6447	$29.9^{+0.6}_{-0.4}$	$29.0^{+0.1}_{-0.1}$	$28.6^{+0.1}_{-0.1}$	$28.7^{+0.1}_{-0.1}$	$28.7^{+0.1}_{-0.1}$
UDF12-3744-6513	$29.2^{+0.3}_{-0.2}$	$28.0^{+0.1}_{-0.1}$	$27.9^{+0.1}_{-0.1}$	$28.1^{+0.1}_{-0.1}$	$28.1^{+0.1}_{-0.1}$
UDF12-4160-7045	$29.6^{+0.4}_{-0.3}$	$28.4^{+0.1}_{-0.1}$	$28.3^{+0.1}_{-0.1}$	$28.3^{+0.1}_{-0.1}$	$28.4^{+0.1}_{-0.1}$
UDF12-4122-7232	>30.1	$29.2^{+0.1}_{-0.1}$	$29.2^{+0.2}_{-0.2}$	$29.6^{+0.3}_{-0.3}$	$29.3^{+0.3}_{-0.2}$
UDF12-3894-7456	>30.1	$29.5^{+0.2}_{-0.2}$	$29.5^{+0.3}_{-0.3}$	>30.2	$29.5^{+0.3}_{-0.3}$
UDF12-4290-7174	>30.1	$29.7^{+0.2}_{-0.2}$	$29.4^{+0.3}_{-0.2}$	$29.8^{+0.4}_{-0.3}$	$30.2^{+0.7}_{-0.4}$
UDF12-4056-6436	$29.8^{+0.5}_{-0.4}$	$28.2^{+0.1}_{-0.1}$	$28.2^{+0.1}_{-0.1}$	$28.2^{+0.1}_{-0.1}$	$28.3^{+0.1}_{-0.1}$
UDF12-4431-6452	$29.6^{+0.4}_{-0.3}$	$28.3^{+0.1}_{-0.1}$	$28.2^{+0.1}_{-0.1}$	$28.2^{+0.1}_{-0.1}$	$28.4^{+0.1}_{-0.1}$
UDF12-3958-6565	$29.5^{+0.4}_{-0.3}$	$28.0^{+0.1}_{-0.1}$	$28.0^{+0.1}_{-0.1}$	$27.9^{+0.1}_{-0.1}$	$28.0^{+0.1}_{-0.1}$
UDF12-4037-6560	>30.1	$29.5^{+0.2}_{-0.2}$	$29.3^{+0.3}_{-0.2}$	$29.7^{+0.4}_{-0.3}$	$29.7^{+0.4}_{-0.3}$
UDF12-4019-6190	>30.1	$29.4^{+0.2}_{-0.1}$	$29.7^{+0.4}_{-0.3}$	$29.5^{+0.3}_{-0.2}$	$29.4^{+0.3}_{-0.2}$
UDF12-4422-6337	>30.0	$29.7^{+0.3}_{-0.2}$	>30.2	$29.5^{+0.4}_{-0.3}$	$30.2^{+0.8}_{-0.4}$
UDF12-4472-6362	>30.0	$28.7^{+0.2}_{-0.1}$	$29.0^{+0.3}_{-0.2}$	$28.3^{+0.2}_{-0.2}$	$28.3^{+0.1}_{-0.1}$
UDF12-4263-6416	>30.0	$29.7^{+0.2}_{-0.2}$	$29.7^{+0.4}_{-0.3}$	$30.0^{+0.6}_{-0.4}$	$29.8^{+0.4}_{-0.3}$
UDF12-4484-6568	>30.0	$28.9^{+0.2}_{-0.2}$	$29.5^{+0.6}_{-0.4}$	$29.0^{+0.4}_{-0.3}$	$29.2^{+0.4}_{-0.3}$
UDF12-3975-7451	>30.1	$29.0^{+0.1}_{-0.1}$	$29.2^{+0.2}_{-0.2}$	$28.8^{+0.2}_{-0.1}$	$29.0^{+0.2}_{-0.2}$
UDF12-3989-6189	$30.1^{+0.8}_{-0.5}$	$29.0^{+0.1}_{-0.1}$	$28.9^{+0.2}_{-0.1}$	$29.0^{+0.2}_{-0.2}$	$29.1^{+0.2}_{-0.2}$
UDF12-3729-6175	>30.1	$28.9^{+0.1}_{-0.1}$	$28.7^{+0.1}_{-0.1}$	$28.8^{+0.2}_{-0.1}$	$28.5^{+0.1}_{-0.1}$
UDF12-3456-6494	>30.1	$29.2^{+0.1}_{-0.1}$	$29.1^{+0.2}_{-0.2}$	$28.9^{+0.2}_{-0.2}$	$28.8^{+0.1}_{-0.1}$
UDF12-4068-6498	>30.1	$29.3^{+0.2}_{-0.1}$	$29.0^{+0.2}_{-0.2}$	$29.0^{+0.2}_{-0.2}$	$29.2^{+0.2}_{-0.2}$
UDF12-3692-6516	>30.1	$29.6^{+0.2}_{-0.2}$	$29.5^{+0.3}_{-0.2}$	$29.3^{+0.3}_{-0.2}$	$29.9^{+0.5}_{-0.3}$

Table A2 – *continued*

Name	z_{850}	Y_{105}	J_{125}	J_{140}	H_{160}
UDF12-4071-7347	>30.1	$29.3^{+0.1}_{-0.1}$	$29.6^{+0.4}_{-0.3}$	$29.0^{+0.2}_{-0.2}$	$29.7^{+0.4}_{-0.3}$
UDF12-4036-8022	>30.1	$29.7^{+0.2}_{-0.2}$	$29.7^{+0.4}_{-0.3}$	$29.5^{+0.3}_{-0.3}$	$30.2^{+0.8}_{-0.5}$
UDF12-3755-6019	>30.1	$29.5^{+0.2}_{-0.2}$	$29.3^{+0.2}_{-0.2}$	$29.6^{+0.3}_{-0.3}$	$29.2^{+0.2}_{-0.2}$
UDF12-4256-6566	$28.9^{+0.2}_{-0.2}$	$26.9^{+0.1}_{-0.1}$	$26.7^{+0.1}_{-0.1}$	$26.6^{+0.1}_{-0.1}$	$26.5^{+0.1}_{-0.1}$
UDF12-4105-7156	$30.0^{+0.7}_{-0.4}$	$28.3^{+0.1}_{-0.1}$	$28.0^{+0.1}_{-0.1}$	$27.9^{+0.1}_{-0.1}$	$28.0^{+0.1}_{-0.1}$
UDF12-3853-7519	>30.1	$29.2^{+0.1}_{-0.1}$	$29.0^{+0.2}_{-0.2}$	$29.0^{+0.2}_{-0.2}$	$29.3^{+0.3}_{-0.2}$
UDF12-3825-6566	>30.1	$29.7^{+0.2}_{-0.2}$	$29.8^{+0.4}_{-0.3}$	$29.2^{+0.2}_{-0.2}$	$29.4^{+0.3}_{-0.2}$
UDF12-3836-6119	$29.8^{+0.6}_{-0.4}$	$28.5^{+0.1}_{-0.1}$	$28.0^{+0.1}_{-0.1}$	$28.3^{+0.1}_{-0.1}$	$28.2^{+0.1}_{-0.1}$
UDF12-3709-6441	>30.1	$30.1^{+0.3}_{-0.3}$	$30.1^{+0.6}_{-0.4}$	$30.1^{+0.6}_{-0.4}$	$29.8^{+0.4}_{-0.3}$
UDF12-3402-6504	>30.1	$28.9^{+0.1}_{-0.1}$	$28.4^{+0.1}_{-0.1}$	$28.5^{+0.1}_{-0.1}$	$28.8^{+0.1}_{-0.1}$
UDF12-4384-6311	>30.0	$29.5^{+0.2}_{-0.2}$	$29.1^{+0.2}_{-0.2}$	$29.0^{+0.2}_{-0.2}$	$29.5^{+0.3}_{-0.2}$
UDF12-4256-7314	$29.8^{+0.6}_{-0.4}$	$27.7^{+0.1}_{-0.1}$	$27.4^{+0.1}_{-0.1}$	$27.4^{+0.1}_{-0.1}$	$27.3^{+0.1}_{-0.1}$
UDF12-4035-7468	>30.0	$29.8^{+0.3}_{-0.2}$	$29.3^{+0.3}_{-0.2}$	$29.7^{+0.4}_{-0.3}$	$29.8^{+0.4}_{-0.3}$
UDF12-3973-6214	>30.1	$28.9^{+0.1}_{-0.1}$	$28.4^{+0.1}_{-0.1}$	$28.9^{+0.2}_{-0.1}$	$28.8^{+0.1}_{-0.1}$
UDF12-3668-8067	>30.1	$29.2^{+0.2}_{-0.1}$	$28.9^{+0.2}_{-0.2}$	$28.7^{+0.2}_{-0.1}$	$29.3^{+0.3}_{-0.2}$
UDF12-3708-8092	>30.1	$29.8^{+0.3}_{-0.2}$	$29.5^{+0.4}_{-0.3}$	$29.4^{+0.3}_{-0.2}$	$29.5^{+0.4}_{-0.3}$
UDF12-4242-6243	>30.1	$29.0^{+0.1}_{-0.1}$	$28.6^{+0.1}_{-0.1}$	$28.5^{+0.1}_{-0.1}$	$28.5^{+0.1}_{-0.1}$
UDF12-3431-7115	>30.1	$28.8^{+0.1}_{-0.1}$	$28.4^{+0.1}_{-0.1}$	$28.4^{+0.1}_{-0.1}$	$28.1^{+0.1}_{-0.1}$
UDF12-3868-5477	>30.1	$30.1^{+0.4}_{-0.3}$	$30.0^{+0.5}_{-0.3}$	$29.8^{+0.5}_{-0.3}$	$29.9^{+0.4}_{-0.3}$
UDF12-4242-6137	>30.1	$29.3^{+0.2}_{-0.2}$	$29.1^{+0.3}_{-0.2}$	$28.7^{+0.2}_{-0.2}$	$28.8^{+0.2}_{-0.2}$
UDF12-4100-7216	>30.1	$30.1^{+0.3}_{-0.3}$	$29.6^{+0.4}_{-0.3}$	$29.6^{+0.4}_{-0.3}$	>30.2
UDF12-4239-6243	$29.6^{+0.4}_{-0.3}$	$28.8^{+0.1}_{-0.1}$	$28.8^{+0.2}_{-0.1}$	$28.5^{+0.1}_{-0.1}$	$28.7^{+0.1}_{-0.1}$
UDF12-4314-6285	>30.1	$28.6^{+0.1}_{-0.1}$	$27.9^{+0.1}_{-0.1}$	$27.8^{+0.1}_{-0.1}$	$27.7^{+0.1}_{-0.1}$
UDF12-3313-6545	>30.1	$28.9^{+0.1}_{-0.1}$	$28.5^{+0.1}_{-0.1}$	$28.2^{+0.1}_{-0.1}$	$28.6^{+0.1}_{-0.1}$
UDF12-3885-7540	>30.1	$29.4^{+0.2}_{-0.1}$	$28.9^{+0.2}_{-0.2}$	$28.8^{+0.2}_{-0.1}$	$28.9^{+0.2}_{-0.2}$
UDF12-3931-6181	>30.1	$29.4^{+0.2}_{-0.2}$	$28.7^{+0.1}_{-0.1}$	$28.8^{+0.2}_{-0.1}$	$29.2^{+0.2}_{-0.2}$
UDF12-4334-6252	>30.0	$30.2^{+0.5}_{-0.3}$	$29.4^{+0.3}_{-0.2}$	$29.5^{+0.4}_{-0.3}$	$30.2^{+0.7}_{-0.4}$
UDF12-4308-6242	>30.0	$29.9^{+0.3}_{-0.2}$	$29.3^{+0.3}_{-0.2}$	$29.5^{+0.4}_{-0.3}$	$29.2^{+0.2}_{-0.2}$
UDF12-3880-7072	>30.1	$27.6^{+0.1}_{-0.1}$	$27.0^{+0.1}_{-0.1}$	$26.9^{+0.1}_{-0.1}$	$26.8^{+0.1}_{-0.1}$
UDF12-4281-6505	>30.1	$30.1^{+0.3}_{-0.3}$	$29.2^{+0.2}_{-0.2}$	$29.3^{+0.3}_{-0.2}$	$28.9^{+0.2}_{-0.1}$
UDF12-4288-6345	>30.0	$28.9^{+0.1}_{-0.1}$	$28.1^{+0.1}_{-0.1}$	$28.2^{+0.1}_{-0.1}$	$27.9^{+0.1}_{-0.1}$
UDF12-4470-6443	>30.0	$28.1^{+0.1}_{-0.1}$	$27.4^{+0.1}_{-0.1}$	$27.4^{+0.1}_{-0.1}$	$27.4^{+0.1}_{-0.1}$
UDF12-4033-8026	>30.1	$29.7^{+0.2}_{-0.2}$	$28.9^{+0.2}_{-0.2}$	$29.2^{+0.2}_{-0.2}$	$29.0^{+0.2}_{-0.2}$
UDF12-3722-8061	>30.1	$28.6^{+0.1}_{-0.1}$	$27.9^{+0.1}_{-0.1}$	$27.9^{+0.1}_{-0.1}$	$27.9^{+0.1}_{-0.1}$
UDF12-4474-6449	>30.0	$29.4^{+0.2}_{-0.2}$	$28.6^{+0.1}_{-0.1}$	$28.5^{+0.1}_{-0.1}$	$28.8^{+0.1}_{-0.1}$
UDF12-4240-6550	>30.1	$30.0^{+0.3}_{-0.2}$	$29.0^{+0.2}_{-0.2}$	$29.3^{+0.3}_{-0.2}$	$29.1^{+0.2}_{-0.2}$
UDF12-3939-7040	>30.1	$29.7^{+0.2}_{-0.2}$	$28.7^{+0.1}_{-0.1}$	$28.6^{+0.1}_{-0.1}$	$28.5^{+0.1}_{-0.1}$
UDF12-3911-6493	>30.1	$30.0^{+0.3}_{-0.2}$	$29.0^{+0.2}_{-0.2}$	$29.1^{+0.2}_{-0.2}$	$29.2^{+0.2}_{-0.2}$
UDF12-3344-6598	>30.1	$29.9^{+0.3}_{-0.2}$	$28.9^{+0.2}_{-0.1}$	$29.0^{+0.2}_{-0.2}$	$29.0^{+0.2}_{-0.2}$
UDF12-3952-7174	>30.0	$28.9^{+0.1}_{-0.1}$	$27.9^{+0.1}_{-0.1}$	$27.8^{+0.1}_{-0.1}$	$27.6^{+0.1}_{-0.1}$
UDF12-4308-6277	>30.0	$29.8^{+0.3}_{-0.2}$	$28.5^{+0.1}_{-0.1}$	$29.0^{+0.2}_{-0.2}$	$28.9^{+0.2}_{-0.1}$
UDF12-3780-6001	>30.1	$29.4^{+0.2}_{-0.2}$	$28.2^{+0.1}_{-0.1}$	$28.3^{+0.1}_{-0.1}$	$28.3^{+0.1}_{-0.1}$
UDF12-3917-5449	>30.1	>30.6	$29.4^{+0.3}_{-0.2}$	>30.1	$29.7^{+0.4}_{-0.3}$
UDF12-3762-6011	>30.1	>30.7	$29.1^{+0.2}_{-0.2}$	$29.4^{+0.3}_{-0.2}$	$29.4^{+0.3}_{-0.2}$
UDF12-3813-5540	>30.1	$29.7^{+0.2}_{-0.2}$	$28.2^{+0.1}_{-0.1}$	$28.1^{+0.1}_{-0.1}$	$28.0^{+0.1}_{-0.1}$
UDF12-3763-6015	>30.1	$30.2^{+0.4}_{-0.3}$	$28.5^{+0.1}_{-0.1}$	$28.5^{+0.1}_{-0.1}$	$28.4^{+0.1}_{-0.1}$
UDF12-3947-8076	>30.1	$30.7^{+0.7}_{-0.4}$	$29.1^{+0.2}_{-0.2}$	$28.6^{+0.1}_{-0.1}$	$28.6^{+0.1}_{-0.1}$
UDF12-3921-6322	>30.1	>30.8	$29.5^{+0.3}_{-0.2}$	$29.2^{+0.2}_{-0.2}$	$29.5^{+0.3}_{-0.2}$
UDF12-4344-6547	>30.1	>30.8	$29.6^{+0.4}_{-0.3}$	$29.8^{+0.4}_{-0.3}$	$29.7^{+0.4}_{-0.3}$
UDF12-4265-7049	>30.1	>30.8	$30.2^{+0.7}_{-0.4}$	$29.5^{+0.3}_{-0.2}$	$29.3^{+0.2}_{-0.2}$
UDF12-3954-6285	>30.1	>30.8	>30.2	>30.2	$28.9^{+0.2}_{-0.1}$

Table A3. Candidate $z \geq 6.5$ galaxies in HUDF09-1. Column 1 lists the candidate names and columns 2 and 3 list the coordinates. Columns 4 and 5 list the best-fitting photometric redshift and the corresponding 1σ uncertainty. Column 6 lists the total absolute UV magnitude, measured using a top-hat filter at 1500 Å in the rest frame of the best-fitting galaxy SED template. Columns 7–10 list the apparent magnitudes in the z_{850}, Y_{105}, J_{125} & H_{160} bands, which have been corrected to total magnitudes assuming a point source. Detections which are less significant than 2σ are listed as the appropriate 2σ limit (all candidates are detected at less than 2σ significance in the V_{606} and i_{775} filters). Column 11 gives references to previous discoveries of objects: (1) Bouwens et al. (2011b), (2) Bouwens et al. (2011b) potential, (3) Wilkins et al. (2011) and (4) Lorenzoni et al. (2011).

Name	RA(J2000)	Dec.(J2000)	$z_{\rm phot}$	Δz	M_{1500}	z_{850}	Y_{105}	J_{125}	H_{160}	References
HUDF09-1_40133	03:32:56.29	−27:40:59.8	6.5	6.4–6.7	−18.7	$29.1^{+0.4}_{-0.3}$	$28.0^{+0.1}_{-0.1}$	$28.1^{+0.2}_{-0.1}$	$28.7^{+0.4}_{-0.3}$	
HUDF09-1_40220	03:32:56.11	−27:41:20.3	6.5	6.3–6.8	−18.3	$29.4^{+0.6}_{-0.4}$	$28.5^{+0.2}_{-0.2}$	$28.5^{+0.2}_{-0.2}$	>29.2	
HUDF09-1_30312	03:33:02.09	−27:41:46.2	6.6	6.5–6.8	−19.6	$28.4^{+0.2}_{-0.2}$	$27.3^{+0.1}_{-0.1}$	$27.3^{+0.1}_{-0.1}$	$27.4^{+0.1}_{-0.1}$	
HUDF09-1_30328	03:33:02.13	−27:42:00.4	6.7	6.4–7.0	−18.6	$29.5^{+0.7}_{-0.4}$	$28.3^{+0.2}_{-0.2}$	$28.3^{+0.2}_{-0.2}$	$28.1^{+0.2}_{-0.2}$	1
HUDF09-1_40096	03:32:56.95	−27:40:50.4	6.7	6.5–7.0	−18.9	$29.1^{+0.4}_{-0.3}$	$28.1^{+0.2}_{-0.1}$	$27.9^{+0.1}_{-0.1}$	$28.2^{+0.3}_{-0.2}$	1
HUDF09-1_30126	03:32:58.99	−27:40:50.0	6.9	6.8–7.2	−19.6	$29.1^{+0.4}_{-0.3}$	$27.5^{+0.1}_{-0.1}$	$27.3^{+0.1}_{-0.1}$	$27.3^{+0.1}_{-0.1}$	1
HUDF09-1_30292	03:33:02.43	−27:41:31.2	7.0	6.8–7.2	−19.5	$29.3^{+0.5}_{-0.3}$	$27.6^{+0.1}_{-0.1}$	$27.4^{+0.1}_{-0.1}$	$27.4^{+0.1}_{-0.1}$	1, 3
HUDF09-1_40030	03:32:58.74	−27:40:21.5	7.0	6.7–7.2	−18.6	>29.6	$28.4^{+0.2}_{-0.2}$	$28.4^{+0.2}_{-0.2}$	$28.6^{+0.4}_{-0.3}$	1
HUDF09-1_40181	03:33:03.81	−27:41:12.3	7.0	6.7–7.2	−18.6	>29.6	$28.3^{+0.2}_{-0.2}$	$28.5^{+0.2}_{-0.2}$	$28.6^{+0.4}_{-0.3}$	1
HUDF09-1_40131	03:33:07.29	−27:41:00.1	7.1	6.7–7.5	−18.3	>29.6	$28.8^{+0.3}_{-0.2}$	$28.5^{+0.2}_{-0.2}$	>29.2	1
HUDF09-1_30085	03:32:59.71	−27:40:35.0	7.1	7.0–7.3	−19.9	$29.4^{+0.6}_{-0.4}$	$27.3^{+0.1}_{-0.1}$	$27.0^{+0.1}_{-0.1}$	$27.1^{+0.1}_{-0.1}$	3
HUDF09-1_30185	03:32:57.82	−27:41:06.5	7.1	6.8–7.5	−18.6	>29.6	$28.5^{+0.2}_{-0.2}$	$28.4^{+0.2}_{-0.2}$	$28.3^{+0.3}_{-0.2}$	1
HUDF09-1_30239	03:32:59.59	−27:41:20.6	7.1	6.9–7.3	−19.6	>29.6	$27.6^{+0.1}_{-0.1}$	$27.4^{+0.1}_{-0.1}$	$27.4^{+0.1}_{-0.1}$	3
HUDF09-1_40037	03:32:58.53	−27:40:23.5	7.1	6.9–7.3	−19.4	>29.6	$27.8^{+0.1}_{-0.1}$	$27.6^{+0.1}_{-0.1}$	$27.7^{+0.1}_{-0.1}$	1, 3
HUDF09-1_30206	03:32:56.71	−27:41:07.7	7.4	7.1–7.6	−19.9	>29.6	$27.6^{+0.1}_{-0.1}$	$27.1^{+0.1}_{-0.1}$	$27.1^{+0.1}_{-0.1}$	2, 3
HUDF09-1_40098	03:32:57.87	−27:40:51.5	7.4	6.9–7.9	−18.4	>29.6	$29.0^{+0.4}_{-0.3}$	$28.5^{+0.2}_{-0.2}$	$28.9^{+0.5}_{-0.4}$	1
HUDF09-1_30232	03:32:59.73	−27:41:19.0	7.5	7.2–7.7	−19.5	>29.6	$28.0^{+0.1}_{-0.1}$	$27.6^{+0.1}_{-0.1}$	$27.5^{+0.1}_{-0.1}$	1
HUDF09-1_40253	03:32:57.52	−27:41:29.9	7.5	7.1–7.9	−18.6	>29.6	$28.8^{+0.4}_{-0.3}$	$28.4^{+0.2}_{-0.2}$	$28.7^{+0.4}_{-0.3}$	1
HUDF09-1_30186	03:32:55.76	−27:41:06.4	7.5	7.2–7.8	−19.5	>29.6	$28.2^{+0.2}_{-0.2}$	$27.6^{+0.1}_{-0.1}$	$27.4^{+0.1}_{-0.1}$	1, 3
HUDF09-1_377	03:32:59.38	−27:42:01.4	7.6	7.3–7.9	−19.1	>29.6	$28.5^{+0.3}_{-0.2}$	$28.0^{+0.1}_{-0.1}$	$27.8^{+0.2}_{-0.1}$	1
HUDF09-1_30132	03:33:04.35	−27:40:51.8	7.6	7.1–8.0	−18.5	>29.4	$29.1^{+0.4}_{-0.3}$	$28.6^{+0.2}_{-0.2}$	$28.5^{+0.3}_{-0.2}$	1
HUDF09-1_30332	03:33:02.82	−27:42:02.3	7.6	7.0–8.0	−18.4	>29.6	$29.2^{+0.5}_{-0.3}$	$28.6^{+0.3}_{-0.2}$	$28.8^{+0.4}_{-0.3}$	1
HUDF09-1_30316	03:33:00.54	−27:41:46.6	7.7	7.3–8.0	−18.8	>29.6	$28.9^{+0.4}_{-0.3}$	$28.3^{+0.2}_{-0.2}$	$28.3^{+0.3}_{-0.2}$	1, 4
HUDF09-1_50298	03:33:02.82	−27:42:10.7	7.7	7.3–7.9	−19.5	>29.6	$28.4^{+0.2}_{-0.2}$	$27.6^{+0.1}_{-0.1}$	$27.4^{+0.1}_{-0.1}$	1
HUDF09-1_30163	03:32:56.45	−27:41:00.3	7.8	7.6–8.0	−19.4	>29.6	$28.5^{+0.2}_{-0.2}$	$27.7^{+0.1}_{-0.1}$	$27.8^{+0.2}_{-0.1}$	1
HUDF09-1_30322	03:33:03.73	−27:41:51.4	7.9	7.5–8.2	−18.9	>29.6	$29.1^{+0.4}_{-0.3}$	$28.1^{+0.2}_{-0.1}$	$28.3^{+0.3}_{-0.2}$	1

Table A4. Candidate $z \geq 6.5$ galaxies in HUDF09-2. Column 1 lists the candidate names and columns 2 and 3 list the coordinates. Columns 4 and 5 list the best-fitting photometric redshift and the corresponding 1σ uncertainty. Column 6 lists the total absolute UV magnitude, measured using a top-hat filter at 1500 Å in the rest frame of the best-fitting galaxy SED template. Columns 7–10 list the apparent magnitudes in the z_{850}, Y_{105}, J_{125} and H_{160} bands, which have been corrected to total magnitudes assuming a point source. Detections which are less significant than 2σ are listed as the appropriate 2σ limit (all candidates are detected at less than 2σ significance in the V_{606} and i_{775} filters). Column 11 gives references to previous discoveries of objects: (1) Bouwens et al. (2011b), (2) Bouwens et al. (2011b) potential, (3) Wilkins et al. (2011) and (4) McLure et al. (2011).

Name	RA(J2000)	Dec.(J2000)	$z_{\rm phot}$	Δz	M_{1500}	z_{850}	Y_{105}	J_{125}	H_{160}	References
HUDF09-2_40134	03:33:05.77	−27:50:55.9	6.5	6.2–6.7	−18.3	$29.3^{+0.5}_{-0.4}$	$28.5^{+0.2}_{-0.2}$	$28.6^{+0.2}_{-0.2}$	$28.8^{+0.4}_{-0.3}$	
HUDF09-2_30262	03:33:00.59	−27:51:49.0	6.6	6.3–6.9	−18.3	>29.6	$28.4^{+0.2}_{-0.2}$	$28.6^{+0.2}_{-0.2}$	$28.4^{+0.3}_{-0.2}$	
HUDF09-2_30274	03:33:09.14	−27:51:53.1	6.6	6.4–6.8	−18.8	$29.3^{+0.5}_{-0.3}$	$28.0^{+0.1}_{-0.1}$	$28.1^{+0.1}_{-0.1}$	$28.0^{+0.2}_{-0.1}$	
HUDF09-2_30224	03:33:00.80	−27:51:32.0	6.6	6.4–6.9	−18.9	$29.0^{+0.4}_{-0.3}$	$28.1^{+0.2}_{-0.1}$	$27.9^{+0.1}_{-0.1}$	$27.9^{+0.2}_{-0.1}$	1
HUDF09-2_40293	03:33:06.57	−27:51:59.8	6.6	6.4–6.8	−18.4	>29.7	$28.3^{+0.2}_{-0.2}$	$28.4^{+0.2}_{-0.1}$	>29.3	1
HUDF09-2_40295	03:33:01.94	−27:52:03.3	6.7	6.5–6.8	−19.6	$28.4^{+0.2}_{-0.1}$	$27.3^{+0.1}_{-0.1}$	$27.3^{+0.1}_{-0.1}$	$27.2^{+0.1}_{-0.1}$	4
HUDF09-2_30085	03:33:09.77	−27:50:48.5	6.9	6.7–7.1	−19.5	$29.2^{+0.5}_{-0.3}$	$27.7^{+0.1}_{-0.1}$	$27.5^{+0.1}_{-0.1}$	$27.2^{+0.1}_{-0.1}$	1, 3
HUDF09-2_40120	03:33:09.64	−27:50:50.8	7.0	6.9–7.1	−20.5	$28.4^{+0.2}_{-0.2}$	$26.5^{+0.1}_{-0.1}$	$26.5^{+0.1}_{-0.1}$	$26.4^{+0.1}_{-0.1}$	3, 4
HUDF09-2_40282	03:33:09.14	−27:51:55.5	7.0	6.8–7.1	−19.7	$29.4^{+0.6}_{-0.4}$	$27.2^{+0.1}_{-0.1}$	$27.3^{+0.1}_{-0.1}$	$27.2^{+0.1}_{-0.1}$	1, 3, 4

Table A4 – *continued*

Name	RA(J2000)	Dec.(J2000)	$z_{\rm phot}$	Δz	M_{1500}	z_{850}	Y_{105}	J_{125}	H_{160}	References
HUDF09-2_40066	03:33:07.34	−27:50:41.8	7.0	6.7–7.4	−18.1	>29.5	$28.7^{+0.3}_{-0.2}$	$29.0^{+0.3}_{-0.2}$	$29.0^{+0.5}_{-0.3}$	
HUDF09-2_10162	03:33:05.40	−27:51:18.9	7.1	6.9–7.3	−19.3	>29.6	$27.9^{+0.1}_{-0.1}$	$27.7^{+0.1}_{-0.1}$	$27.7^{+0.1}_{-0.1}$	1, 3, 4
HUDF09-2_30145	03:33:01.19	−27:51:13.4	7.1	6.9–7.3	−19.5	$29.5^{+0.7}_{-0.4}$	$27.8^{+0.1}_{-0.1}$	$27.5^{+0.1}_{-0.1}$	$27.4^{+0.1}_{-0.1}$	3, 4
HUDF09-2_30132	03:33:03.81	−27:51:03.4	7.1	6.6–7.6	−18.7	>29.5	$28.7^{+0.3}_{-0.2}$	$28.4^{+0.2}_{-0.2}$	$28.0^{+0.2}_{-0.2}$	1
HUDF09-2_40108	03:33:09.71	−27:50:48.6	7.2	6.8–7.5	−18.6	>29.5	$28.7^{+0.3}_{-0.2}$	$28.4^{+0.2}_{-0.1}$	$28.6^{+0.3}_{-0.2}$	1
HUDF09-2_40152	03:33:00.92	−27:51:11.9	7.2	6.8–7.6	−18.2	>29.6	$28.8^{+0.3}_{-0.3}$	$28.8^{+0.3}_{-0.2}$	$28.8^{+0.4}_{-0.3}$	1
HUDF09-2_40020	03:33:07.09	−27:50:21.8	7.2	6.8–7.6	−18.6	>29.5	$28.8^{+0.3}_{-0.2}$	$28.3^{+0.2}_{-0.1}$	$28.8^{+0.4}_{-0.3}$	2
HUDF09-2_10189	03:33:06.39	−27:51:24.8	7.7	7.5–8.0	−18.9	>29.6	$28.9^{+0.3}_{-0.3}$	$28.1^{+0.1}_{-0.1}$	$28.4^{+0.3}_{-0.2}$	1
HUDF09-2_30170	03:33:03.78	−27:51:20.4	7.7	7.6–7.9	−20.6	>29.6	$27.2^{+0.1}_{-0.1}$	$26.5^{+0.1}_{-0.1}$	$26.3^{+0.1}_{-0.1}$	1, 3, 4
HUDF09-2_50096	03:33:04.64	−27:50:53.0	7.8	7.6–7.9	−19.8	>29.5	$28.0^{+0.2}_{-0.1}$	$27.3^{+0.1}_{-0.1}$	$27.3^{+0.1}_{-0.1}$	1, 4
HUDF09-2_10164	03:33:03.76	−27:51:19.7	7.8	7.7–7.9	−20.3	>29.6	$27.6^{+0.1}_{-0.1}$	$26.8^{+0.1}_{-0.1}$	$26.7^{+0.1}_{-0.1}$	1, 4
HUDF09-2_10026	03:33:06.97	−27:50:27.9	8.4	7.9–8.7	−18.8	>29.5	>29.5	$28.5^{+0.2}_{-0.2}$	$28.5^{+0.3}_{-0.2}$	1
HUDF09-2_50121	03:33:03.39	−27:51:00.4	8.4	7.9–8.7	−19.0	>29.5	>29.5	$28.3^{+0.2}_{-0.1}$	$28.2^{+0.2}_{-0.2}$	1
HUDF09-2_50104	03:33:07.58	−27:50:55.1	9.0	8.6–9.2	−19.9	>29.6	>29.6	$27.9^{+0.1}_{-0.1}$	$27.4^{+0.1}_{-0.1}$	1, 4
HUDF09-2_247	03:33:04.24	−27:52:09.4	9.4	9.1–9.6	−19.5	>29.7	>29.6	$28.8^{+0.2}_{-0.2}$	$27.9^{+0.2}_{-0.1}$	1

Table A5. Candidate $z \geq 6.5$ galaxies in ERS. Column 1 lists the candidate names and columns 2 and 3 list the coordinates. Columns 4 and 5 list the best-fitting photometric redshift and the corresponding 1σ uncertainty. Column 6 lists the total absolute UV magnitude, measured using a top-hat filter at 1500 Å in the rest frame of the best-fitting galaxy SED template. Columns 7–10 list the apparent magnitudes in the z_{850}, Y_{098}, J_{125} and H_{160} bands, which have been corrected to total magnitudes assuming a point source. Detections which are less significant than 2σ are listed as the appropriate 2σ limit (all candidates are detected at less than 2σ significance in the B_{435}, V_{606} and i_{775} filters). Column 11 gives references to previous discoveries of objects: (1) Bouwens et al. (2011b), (2) Bouwens et al. (2011b) potential, (3) Wilkins et al. (2011), (4) Lorenzoni et al. (2011) and (5) McLure et al. (2011).

Name	RA(J2000)	Dec.(J2000)	$z_{\rm phot}$	Δz	M_{1500}	z_{850}	Y_{098}	J_{125}	H_{160}	References
ERS_30059	03:32:21.81	−27:44:38.7	6.5	6.2–6.7	−19.8	$28.0^{+0.4}_{-0.3}$	$27.1^{+0.2}_{-0.1}$	$27.1^{+0.1}_{-0.1}$	$26.8^{+0.1}_{-0.1}$	
ERS_50656	03:32:27.01	−27:41:42.9	6.5	6.0–6.8	−19.4	$28.0^{+0.4}_{-0.3}$	$27.4^{+0.2}_{-0.2}$	$27.3^{+0.2}_{-0.1}$	$27.6^{+0.3}_{-0.2}$	2
ERS_30220	03:32:41.39	−27:43:16.9	6.6	6.4–6.8	−20.3	$27.6^{+0.3}_{-0.2}$	$26.6^{+0.1}_{-0.1}$	$26.6^{+0.1}_{-0.1}$	$26.3^{+0.1}_{-0.1}$	2
ERS_30412	03:32:07.86	−27:42:17.8	6.6	6.5–6.9	−20.4	$27.3^{+0.3}_{-0.2}$	$26.7^{+0.1}_{-0.1}$	$26.4^{+0.1}_{-0.1}$	$26.4^{+0.1}_{-0.1}$	5
ERS_30089	03:32:06.83	−27:44:22.2	6.7	6.5–6.8	−20.2	$27.9^{+0.4}_{-0.3}$	$26.6^{+0.1}_{-0.1}$	$26.6^{+0.1}_{-0.1}$	$26.8^{+0.2}_{-0.1}$	1, 5
ERS_30172	03:32:20.24	−27:43:34.3	6.7	6.4–7.0	−19.6	$28.2^{+0.6}_{-0.4}$	$27.4^{+0.2}_{-0.2}$	$27.2^{+0.1}_{-0.1}$	$27.0^{+0.2}_{-0.2}$	2, 5
ERS_30562	03:32:22.52	−27:41:17.4	6.7	6.5–6.9	−19.8	$28.3^{+0.7}_{-0.4}$	$27.1^{+0.2}_{-0.2}$	$27.1^{+0.2}_{-0.1}$	$27.0^{+0.2}_{-0.2}$	1
ERS_30457	03:32:29.54	−27:42:04.5	6.9	6.7–7.0	−20.1	>28.4	$27.0^{+0.2}_{-0.2}$	$26.8^{+0.1}_{-0.1}$	$26.8^{+0.2}_{-0.2}$	1, 3, 5
ERS_30645	03:32:16.00	−27:41:59.1	7.0	6.7–7.2	−19.9	>28.3	$27.5^{+0.3}_{-0.2}$	$27.1^{+0.1}_{-0.1}$	$27.0^{+0.2}_{-0.2}$	1, 5
ERS_30426	03:32:24.09	−27:42:13.8	7.0	6.8–7.2	−20.2	$28.4^{+0.7}_{-0.4}$	$27.2^{+0.2}_{-0.2}$	$26.8^{+0.1}_{-0.1}$	$26.6^{+0.2}_{-0.1}$	1, 3, 5
ERS_30618	03:32:16.19	−27:41:49.8	7.0	6.7–7.2	−19.6	>28.3	$27.7^{+0.4}_{-0.3}$	$27.3^{+0.2}_{-0.2}$	$27.3^{+0.3}_{-0.2}$	1, 5
ERS_10317	03:32:03.21	−27:42:58.1	7.3	7.0–7.6	−19.5	>28.5	>28.2	$27.4^{+0.2}_{-0.2}$	$27.9^{+0.6}_{-0.4}$	
ERS_30100	03:32:11.16	−27:44:16.9	7.4	7.2–7.5	−20.1	>28.3	$28.0^{+0.4}_{-0.3}$	$26.9^{+0.1}_{-0.1}$	$26.9^{+0.2}_{-0.1}$	1
ERS_50207	03:32:35.46	−27:43:23.5	7.4	7.0–7.7	−19.5	>28.5	>28.2	$27.5^{+0.2}_{-0.2}$	$27.6^{+0.4}_{-0.3}$	
ERS_50461	03:32:25.16	−27:41:57.4	7.5	7.3–7.8	−19.8	>28.5	>28.3	$27.2^{+0.2}_{-0.2}$	$27.2^{+0.3}_{-0.2}$	1
ERS_10237	03:32:23.37	−27:43:26.5	8.0	7.6–8.3	−19.8	>28.5	>28.2	$27.1^{+0.2}_{-0.1}$	$27.7^{+0.5}_{-0.3}$	5
ERS_50613	03:32:35.44	−27:41:32.7	8.4	7.5–8.7	−20.0	>28.4	>28.5	$27.2^{+0.2}_{-0.1}$	$27.2^{+0.2}_{-0.2}$	1, 5
ERS_50150	03:32:02.99	−27:43:51.9	8.5	7.7–8.8	−20.3	>28.4	>28.2	$27.0^{+0.1}_{-0.1}$	$26.9^{+0.2}_{-0.2}$	1, 4, 5

Table A6. Candidate $z \geq 6.5$ galaxies in CANDELS GS-DEEP. Column 1 lists the candidate names and columns 2 and 3 list the coordinates. Columns 4 and 5 list the best-fitting photometric redshift and the corresponding 1σ uncertainty. Column 6 lists the total absolute UV magnitude, measured using a top-hat filter at 1500 Å in the rest frame of the best-fitting galaxy SED template. Columns 7–10 list the apparent magnitudes in the z_{850}, Y_{105}, J_{125} and H_{160} bands, which have been corrected to total magnitudes assuming a point source. Detections which are less significant than 2σ are listed as the appropriate 2σ limit (all candidates are detected at less than 2σ significance in the B_{435}, V_{606} and i_{775} filters). Those objects which have significantly deeper z_{850} limits lie within the footprint of the original HUDF ACS imaging. Column 11 gives references to previous discoveries of objects: (1) Oesch et al. (2012b), (2) Yan et al. (2012), (3) Grazian et al. (2012) and (4) Lorenzoni et al. (2013).

Name	RA(J2000)	Dec.(J2000)	$z_{\rm phot}$	Δz	M_{1500}	z_{850}	Y_{105}	J_{125}	H_{160}	References
CGSD_130052	03:32:37.23	−27:45:38.4	6.5	6.4–6.6	−19.7	$28.1^{+0.1}_{-0.1}$	$27.2^{+0.1}_{-0.1}$	$27.1^{+0.1}_{-0.1}$	$27.2^{+0.2}_{-0.2}$	4
CGSD_30322	03:32:22.68	−27:46:09.1	6.6	6.1–7.0	−18.9	>28.6	$27.9^{+0.3}_{-0.2}$	$27.9^{+0.3}_{-0.2}$	$28.0^{+0.5}_{-0.3}$	
CGSD_30157	03:32:37.28	−27:48:54.6	6.7	6.4–7.0	−21.2	$27.6^{+0.1}_{-0.1}$	$26.0^{+0.1}_{-0.1}$	$25.5^{+0.1}_{-0.1}$	$25.5^{+0.1}_{-0.1}$	
CGSD_30134	03:32:14.24	−27:48:55.3	6.8	6.5–7.1	−19.7	>28.6	$27.2^{+0.2}_{-0.2}$	$27.3^{+0.2}_{-0.1}$	$27.1^{+0.2}_{-0.2}$	
CGSD_30237	03:32:28.35	−27:47:34.6	6.8	6.6–7.1	−19.2	>29.8	$27.9^{+0.3}_{-0.2}$	$27.7^{+0.2}_{-0.2}$	$27.8^{+0.4}_{-0.3}$	
CGSD_30261	03:32:40.68	−27:45:11.6	6.9	6.5–7.3	−19.5	>28.5	$27.6^{+0.2}_{-0.2}$	$27.5^{+0.2}_{-0.2}$	$27.2^{+0.2}_{-0.2}$	2
CGSD_30275	03:32:19.94	−27:47:10.6	6.9	6.7–7.2	−19.7	>28.4	$27.2^{+0.2}_{-0.1}$	$27.3^{+0.2}_{-0.1}$	$27.2^{+0.2}_{-0.2}$	3, 4
CGSD_30239	03:32:42.56	−27:47:31.4	7.0	6.7–7.2	−19.5	>30.2	$27.6^{+0.2}_{-0.2}$	$27.4^{+0.2}_{-0.2}$	$27.3^{+0.2}_{-0.2}$	
CGSD_30336	03:32:25.22	−27:46:26.7	7.3	7.1–7.5	−20.2	>28.7	$27.1^{+0.1}_{-0.1}$	$26.7^{+0.1}_{-0.1}$	$26.8^{+0.1}_{-0.1}$	
CGSD_30389	03:32:40.69	−27:44:16.7	7.3	7.1–7.5	−20.2	>28.5	$27.2^{+0.1}_{-0.1}$	$26.8^{+0.1}_{-0.1}$	$26.8^{+0.1}_{-0.1}$	4
CGSD_30146	03:32:23.77	−27:49:13.6	7.3	7.1–7.6	−20.1	>28.6	$27.2^{+0.2}_{-0.2}$	$26.9^{+0.1}_{-0.1}$	$27.0^{+0.2}_{-0.2}$	3
CGSD_30159	03:32:24.33	−27:49:15.0	7.3	7.0–7.6	−19.8	>28.6	$27.5^{+0.3}_{-0.2}$	$27.2^{+0.2}_{-0.1}$	$27.1^{+0.2}_{-0.2}$	1, 3
CGSD_30048	03:32:46.89	−27:50:07.5	7.4	7.2–7.7	−20.4	>28.4	$27.1^{+0.1}_{-0.1}$	$26.7^{+0.1}_{-0.1}$	$26.4^{+0.1}_{-0.1}$	1
CGSD_30284	03:32:27.91	−27:45:42.8	7.4	7.1–7.7	−19.8	>28.8	$27.7^{+0.2}_{-0.2}$	$27.2^{+0.1}_{-0.1}$	$27.6^{+0.3}_{-0.2}$	4
CGSD_30388	03:32:40.26	−27:44:09.9	7.5	7.1–7.8	−19.7	>28.6	$27.8^{+0.2}_{-0.2}$	$27.4^{+0.2}_{-0.2}$	$27.3^{+0.3}_{-0.2}$	1, 4
CGSD_40222	03:32:32.03	−27:45:37.1	7.6	7.4–7.8	−20.6	>28.6	$27.1^{+0.1}_{-0.1}$	$26.5^{+0.1}_{-0.1}$	$26.3^{+0.1}_{-0.1}$	1
CGSD_130048	03:32:44.02	−27:47:27.3	7.7	7.5–7.9	−20.0	>29.7	$27.6^{+0.2}_{-0.2}$	$27.1^{+0.1}_{-0.1}$	$26.9^{+0.2}_{-0.1}$	4
CGSD_30414	03:32:47.95	−27:44:50.4	7.7	7.4–8.0	−19.8	>28.3	$28.1^{+0.3}_{-0.2}$	$27.4^{+0.2}_{-0.2}$	$27.0^{+0.2}_{-0.2}$	2
CGSD_30014	03:32:21.43	−27:52:21.5	7.8	7.4–8.3	−19.5	>28.4	$28.4^{+0.7}_{-0.4}$	$27.5^{+0.2}_{-0.2}$	$27.9^{+0.5}_{-0.3}$	
CGSD_50050	03:32:20.97	−27:51:37.1	7.9	7.6–8.1	−20.0	>28.4	$28.0^{+0.2}_{-0.2}$	$27.1^{+0.1}_{-0.1}$	$26.9^{+0.2}_{-0.1}$	1, 2
CGSD_30337	03:32:14.13	−27:48:28.9	7.9	7.6–8.3	−20.2	>28.5	$27.9^{+0.4}_{-0.3}$	$26.9^{+0.1}_{-0.1}$	$27.1^{+0.2}_{-0.2}$	2, 4
CGSD_10080	03:32:14.21	−27:50:06.9	8.0	7.4–8.3	−19.3	>28.5	>28.4	$27.7^{+0.2}_{-0.2}$	$28.4^{+0.8}_{-0.4}$	
CGSD_50145	03:32:49.94	−27:48:18.1	8.0	7.9–8.1	−21.4	>28.5	$27.0^{+0.1}_{-0.1}$	$25.8^{+0.1}_{-0.1}$	$25.7^{+0.1}_{-0.1}$	1, 2
CGSD_50276	03:32:27.79	−27:45:14.1	8.2	7.8–8.5	−19.7	>28.6	$28.8^{+0.6}_{-0.4}$	$27.4^{+0.2}_{-0.2}$	$27.6^{+0.3}_{-0.3}$	1
CGSD_10023	03:32:16.91	−27:52:01.9	8.2	7.8–8.6	−19.5	>28.5	>28.5	$27.6^{+0.2}_{-0.2}$	$28.1^{+0.6}_{-0.4}$	2
CGSD_50001	03:32:18.19	−27:52:45.6	8.4	8.0–8.6	−20.2	>28.5	>28.6	$27.1^{+0.2}_{-0.1}$	$27.0^{+0.2}_{-0.2}$	1, 2
CGSD_50067	03:32:35.00	−27:49:21.6	8.9	8.7–9.1	−20.3	>28.5	>28.9	$27.3^{+0.2}_{-0.1}$	$27.0^{+0.2}_{-0.1}$	1, 2

Table A7. Candidate $z \geq 6.5$ galaxies in CANDELS GS-WIDE. Column 1 lists the candidate names and columns 2 and 3 list the coordinates. Columns 4 and 5 list the best-fitting photometric redshift and the corresponding 1σ uncertainty. Column 6 lists the total absolute UV magnitude, measured using a top-hat filter at 1500 Å in the rest frame of the best-fitting galaxy SED template. Columns 7–10 list the apparent magnitudes in the z_{850}, Y_{105}, J_{125} and H_{160} bands, which have been corrected to total magnitudes assuming a point source. Detections which are less significant than 2σ are listed as the appropriate 2σ limit (both candidates are detected at less than 2σ significance in the B_{435}, V_{606} and i_{775} filters). Column 11 gives references to previous discoveries of objects.

Name	RA(J2000)	Dec.(J2000)	$z_{\rm phot}$	Δz	M_{1500}	z_{850}	Y_{105}	J_{125}	H_{160}	References
CGSW_30099	03:32:57.39	−27:53:21.8	6.5	6.4–6.6	−20.1	$27.6^{+0.1}_{-0.1}$	$26.6^{+0.2}_{-0.2}$	$26.7^{+0.2}_{-0.2}$	$26.7^{+0.3}_{-0.2}$	
CGSW_30210	03:32:57.62	−27:52:37.4	6.5	6.4–6.7	−20.0	$27.7^{+0.1}_{-0.1}$	$26.6^{+0.2}_{-0.2}$	$27.0^{+0.3}_{-0.2}$	$26.6^{+0.3}_{-0.2}$	

Table A8. Candidate $z \geq 6.5$ galaxies in CANDELS UDS. Column 1 lists the candidate names and columns 2 and 3 list the coordinates. Columns 4 and 5 list the best-fitting photometric redshift and the corresponding 1σ uncertainty. Column 6 lists the total absolute UV magnitude, measured using a top-hat filter at 1500 Å in the rest frame of the best-fitting galaxy SED template. Columns 7–9 list the apparent magnitudes in the i_{814}, J_{125} and H_{160} bands, which have been corrected to total magnitudes assuming a point source. Detections which are less significant than 2σ are listed as the appropriate 2σ limit (all candidates are detected at less than 2σ significance in the V_{606} filter). Column 10 gives references to previous discoveries of objects: (1) Ouchi et al. (2009) and (2) Grazian et al. (2012). We note that CUDS_20114 is an extended, multicomponent, object (Ouchi et al. 2009), and that the photometry reported here is for the central component only.

Name	RA(J2000)	Dec.(J2000)	$z_{\rm phot}$	Δz	M_{1500}	i_{814}	J_{125}	H_{160}	References
CUDS_20144	02:16:54.99	−05:09:11.9	6.5	6.4–6.6	−20.4	>28.7	$26.3^{+0.2}_{-0.1}$	$26.3^{+0.2}_{-0.1}$	2
CUDS_20114	02:17:57.61	−05:08:44.9	6.6	6.5–6.7	−20.8	>28.2	$26.0^{+0.1}_{-0.1}$	$26.1^{+0.1}_{-0.1}$	1, 2
CUDS_20253	02:17:11.61	−05:10:33.7	6.7	6.5–7.0	−20.5	>28.6	$26.3^{+0.2}_{-0.1}$	$26.2^{+0.2}_{-0.1}$	2
CUDS_20482	02:17:39.70	−05:13:50.6	6.8	6.5–7.0	−20.7	>28.6	$26.1^{+0.1}_{-0.1}$	$26.2^{+0.1}_{-0.1}$	2
CUDS_20450	02:17:15.43	−05:13:23.7	7.1	6.9–7.4	−20.3	>28.7	$26.8^{+0.2}_{-0.2}$	$26.5^{+0.2}_{-0.2}$	
CUDS_20398	02:16:56.13	−05:12:36.1	7.2	7.1–7.3	−21.1	>28.7	$25.9^{+0.1}_{-0.1}$	$25.9^{+0.1}_{-0.1}$	2
CUDS_20615	02:17:41.33	−05:15:33.4	7.4	7.1–7.7	−21.0	>28.3	$26.1^{+0.1}_{-0.1}$	$25.8^{+0.1}_{-0.1}$	2

Table A9. Candidate $z \geq 6.5$ galaxies in BoRG. Column 1 lists the candidate names and columns 2 and 3 list the coordinates. Columns 4 and 5 list the best-fitting photometric redshift and the corresponding 1σ uncertainty. Column 6 lists the total absolute UV magnitude, measured using a top-hat filter at 1500 Å in the rest frame of the best-fitting galaxy SED template. Columns 7–9 list the apparent magnitudes in the Y_{098}, J_{125} and H_{160} bands, which have been corrected to total magnitudes assuming a point source. Detections which are less significant than 2σ are listed as the appropriate 2σ limit (all candidates are detected at less than 2σ significance in the V_{606} or V_{600} filters). Column 10 gives references to previous discoveries of objects: (1) Bradley et al. (2012).

Name	RA(J2000)	Dec.(J2000)	$z_{\rm phot}$	Δz	M_{1500}	Y_{098}	J_{125}	H_{160}	References
BoRG_54	08:35:13.61	+24:55:36.2	7.6	7.4–7.8	−20.7	>28.0	$26.3^{+0.1}_{-0.1}$	$26.5^{+0.3}_{-0.2}$	1
BoRG_120	22:02:46.32	+18:51:29.5	7.7	7.3–8.0	−20.4	>28.8	$26.6^{+0.2}_{-0.1}$	$26.7^{+0.2}_{-0.2}$	1
BoRG_118	22:02:50.37	+18:50:21.0	8.3	7.5–8.8	−20.4	>28.8	$26.9^{+0.2}_{-0.2}$	$26.9^{+0.3}_{-0.2}$	
BoRG_51	04:39:46.95	−52:43:55.2	8.4	7.6–8.8	−21.4	>28.6	$26.0^{+0.1}_{-0.1}$	$25.9^{+0.1}_{-0.1}$	1

This paper has been typeset from a TEX/LATEX file prepared by the author.